

University of Cincinnati

Date: 7/15/2015

I. Zaid Al-Shammaa , hereby submit this original work as part of the requirements for the degree of Master of Science in Pharmaceutical Sciences.

It is entitled:

Targeting Drug-Resistant Tuberculosis Using SMART Nanotechnology Approach

Student's name: **Zaid Al-Shammaa**

This work and its defense approved by:

Committee chair: Giovanni Pauletti, Ph.D.

Committee member: Gary Thompson, Ph.D.

Committee member: Kevin Li, Ph.D.



18398

Targeting Drug-Resistant Tuberculosis Using SMART Nanotechnology

Approach

A thesis submitted to the

Graduate School of the University of Cincinnati

In partial fulfillment of the requirements for the degree of

MASTER OF SCIENCE

Graduate Program in Pharmaceutical Sciences

at the James L. Winkle College of Pharmacy

August 2015

by

Zaid Taha Hamoudi Al-shammaa

B.S. (Pharmacy), Al-Mustansiriyah University, Iraq 2006

Committee Chair: Dr. Giovanni M. Pauletti

Abstract

Stimulus-induced drug delivery systems and nanotechnology allow selective targeting of disease-affected tissues in order to improve pharmacokinetic properties of therapeutics while minimizing adverse events associated with systemic exposure. The objective of this research was to explore Eudragit L-100, a pH sensitive co-polymer comprised of methacrylic acid and methyl methacrylate, in the fabrication of nanoparticles (NPs) that efficiently accumulate in alveolar macrophages and preferentially release the payload in *Mycobacteria tuberculosis* (TB)-infected lysosomes. The lipophilic fluorescent dye Rhodamine123 (Rh123) was selected as a surrogate for the anti-TB agent rifampicin. Eudragit L-100 NPs were prepared using the nanoprecipitation technique, which afforded colloids with a hydrodynamic diameter between 238-270 nm and a zeta potential ranging from -21.8 to -33.1 mV. Subsequent *in vitro* release experiments performed in phosphate-buffered saline at pH 5.5, 6.2 and 7.4 demonstrated pH-dependent release kinetics of Rh123 from NPs. In comparison to pH 5.5, the cumulative amount of Rh123 released was approximately 3-fold greater at pH 6.2 and 6-fold increased at pH 7.4. Regression analyses using various mathematical models suggested predominant contribution of passive diffusion in Rh123 release at pH 5.5, with increasing assistance of carrier erosion at pH 6.2 and 7.4. Incubation of the mouse alveolar macrophage (MH-S) cell line with Rh123-containing NPs revealed a 50% decrease in cellular viability at NP concentrations of 2.8 mg/mL. Consequently, cellular uptake experiments were performed using a NP concentration of 1.62 mg/mL where viability $> 99.9\%$ was guaranteed. To simulate less acidic lysosomal pH conditions of TB-infected macrophages, MH-S cells were exposed to NH_4Cl concentrations up to 100 mM. Only the highest NH_4Cl concentration increased the lysosomal pH of MH-S cells from resting pH 5.5 to the desired pH 6.2. Cellular uptake of Rh123-containing Eudragit L-100

NPs was assessed spectrophotometrically using NH_4Cl - and vehicle-treated control cells. Interestingly, intracellular Rh123 concentrations were significantly decreased in NH_4Cl -treated cells. As confocal microscopy was unable to distinguish intracellular distribution pattern between NP-associated and dissolved Rh123, alternative methodologies must be explored to determine whether less acidic lysosomal pH alters the release of Eudragit L-100 NP payload in TB-infected macrophages.

Acknowledgement

I would like to thank all the members who made the journey through graduate school enjoyable and this thesis possible.

I would like to thank my advisor Dr. Giovanni M. Pauletti for his patience, help and efforts to explain things clearly and guiding me through the graduate study. I appreciate Dr. Gary A. Thompson for his valuable inputs on my thesis, especially his comments and suggestions about regression analysis and mathematical model fitting. I am also thankful for Dr. Kevin Li for his help and being a member of my committee.

I am indebted to my lab mates Dr. Sarah Potter, Ayat, Noura, Basma and Nermin for training me on several experiments and helping me in every way possible.

To Ganesh, Daniah, Harikrishna and all my other friends whom I met during my stay at UC, I am grateful for their help and support.

I would like to thank the Higher Committee for Education Development in Iraq (HCED) for offering me the chance to study in the U.S. and their financial support.

Finally to my Mom, Dad, and Ali for their prayers and for encouraging and believing in me at all the times. I would not have made it without you.

TABLE OF CONTENTS

1. Introduction	8
1.1. The Threat of Tuberculosis in the 21st Century	8
1.1.1. Tuberculosis Prevalence and Pathogenicity.....	8
1.1.2. Therapeutic Strategies	10
1.2. The Role of Alveolar Macrophages in Pulmonary Immune Defense	13
1.2.1. Molecular Aspects of <i>M. tuberculosis</i> Interaction with Alveolar Macrophages ..	16
1.2.2. Interference of <i>M. tuberculosis</i> with Alveolar Macrophages Clearance	17
1.3. Drug Delivery Technology to Manage Tuberculosis.....	19
1.3.1. Conventional Drug Delivery Systems used in TB.....	19
1.3.2. SMART Drug Delivery Systems	20
2. Research Objective.....	25
2.1. Hypothesis	25
2.2. Specific Aims.....	25
3. Materials and Methods	26
3.1. Materials.....	26
3.2. Cell Culture.....	26
3.3. Fabrication of Eudragit L-100 Nanoparticles.....	27
3.4. Physical Properties of the Nanoparticles.....	28
3.5. Rhodamine123 Encapsulation Efficiency.....	28

3.6. Rh123 Release <i>In vitro</i>	29
3.7. Cells Viability.....	33
3.8. Cellular Uptake Studies	34
3.9. BCA Cellular Protein Quantification Assay	35
3.10. Lysosomal pH	36
3.11. Simulated Lysosomal Conditions of TB-infected Alveolar Macrophages	37
3.12. Confocal Microscope.....	37
3.13. Statistical Analysis.....	38
4. Results.....	39
4.1. Eudragit L-100 Nanoparticles.....	39
4.1.1. Physicochemical Properties of Eudragit L-100 Nanoparticles.....	39
4.1.2. Rhodamine123 Encapsulation Efficiency.....	40
4.1.3. Release Kinetics of Rh123 from Eudragit L-100 NP.....	46
4.2. Alveolar Macrophages Cell Culture Model	48
4.2.1. Cell Viability Studies.....	50
4.2.2. Nanoparticles Uptake by Alveolar Macrophages.....	52
4.2.3. Modulation of Lysosomal pH Values.....	54
4.2.4. Lysosomal pH Effect on Nanoparticles Uptake in MH-S Cells.....	61
5. Discussion	65
6. Conclusions	72

7. Future Directions..... 73

8. References 75

APPENDIX 83

LIST OF FIGURES

Fig. 1: Cell wall structure of <i>Mycobacterium tuberculosis</i>	9
Fig. 2: Mechanism of action of first-line anti-TB drugs	11
Fig. 3: Biochemical pathway of phagosome acidification in macrophages	14
Fig. 4: pH-dependent dissolution of Eudragit polymers.....	22
Fig. 5: Optimization of NP size	39
Fig. 6: Effect of different mixing techniques on NP size distribution	41
Fig. 7: Effect of different solvents on NP size distribution	42
Fig. 8: Effect of NaOH on Eudragit L-100 NP particle size distribution	43
Fig. 9: Dissolution of Rh123-containing Eudragit L-100 NPs kinetics	44
Fig. 10: pH-dependent release of Rh123 from Eudragit L-100 NPs	46
Fig. 11: Optimization of MH-S cells attachment	49
Fig. 12: Cytotoxicity of Eudragit L-100 nanoparticles on MH-S cells <i>in vitro</i>	51
Fig. 13: Uptake of Rh123-containing Eudragit L-100 NPs in MH-S cells	53
Fig. 14: pH-dependent fluorescence of FD40	54
Fig. 15: FD40 uptake kinetics in MH-S cells	56
Fig. 16: Quenching efficiency of FD40 using Trypan blue	57

Fig. 17: Estimation of lysosomal pH in MH-S cells	58
Fig. 18: Lysosomal pH modulation in MH-S cells	60
Fig. 19: Effect of lysosomal pH on internalization efficiency	62
Fig. 20: Visualization of cellular uptake of Rh123-Eudragit L-100 NPs	63

LIST OF TABLES

Table 1: Conventional Dose Regimens of Anti-TB Drugs	12
Table 2: Overview of Stimulus-induced SMART Drug Delivery Systems	21
Table 3: Physical Characteristics of Eudragit L-100 NPs	45
Table 4: Mathematical Assessment of Rh123 Release Kinetics	47
Table 5: Effect of Eudragit L-100 Nanoparticles on MH-S Cell Viability <i>in vitro</i>	52

LIST OF ABBREVIATIONS

AM	Alveolar macrophages
ddH ₂ O	Deionized distilled water
DLS	Dynamic laser light scattering
DMEM	Dulbecco's modified Eagle medium
E.E.	Payload encapsulation efficiency in nanoparticles
EM	Emission wavelength
EX	Excitation wavelength
FD40	Fluorescein isothiocyanate-labeled dextran (M.W. = 40,000 Da)
L.C.	Loading capacity of nanoparticles
MDR	Multidrug resistance
MH-S	Mouse alveolar macrophage cell line
NP	Nanoparticle
PBS	Phosphate-buffered saline
Rh123	Rhodamine 123
SD	Standard deviation
TB	Tuberculosis

1. Introduction

1.1. The Threat of Tuberculosis in the 21st Century

1.1.1. Tuberculosis Prevalence and Pathogenicity

Tuberculosis (TB) is one of the deadliest diseases around the world. According to the U.S. Center of Disease Control and Prevention (CDC), approximately 9 million cases were reported in 2013 worldwide, which resulted in estimated 1.5 million tuberculosis-related deaths. In the same year, 9,582 TB cases were reported in the U.S., which translates into an incidence rate of 3.0 cases per 100,000 people (CDC, 2013). Tuberculosis is a bacterial infection caused by the rod-shaped *Mycobacterium tuberculosis* bacillus. Unlike other pathogenic bacteria, TB bacilli possess a unique cell envelope composed of complex lipids contributing to ~60% of their total weight (Torrelles et al., 2010). The complex cell envelope of *M. tuberculosis* can be divided into two main structures: the capsule-like outermost layer and cell wall (Brennan, 2003). A schematic structure of the *M. tuberculosis* cell wall is shown in Figure 1.

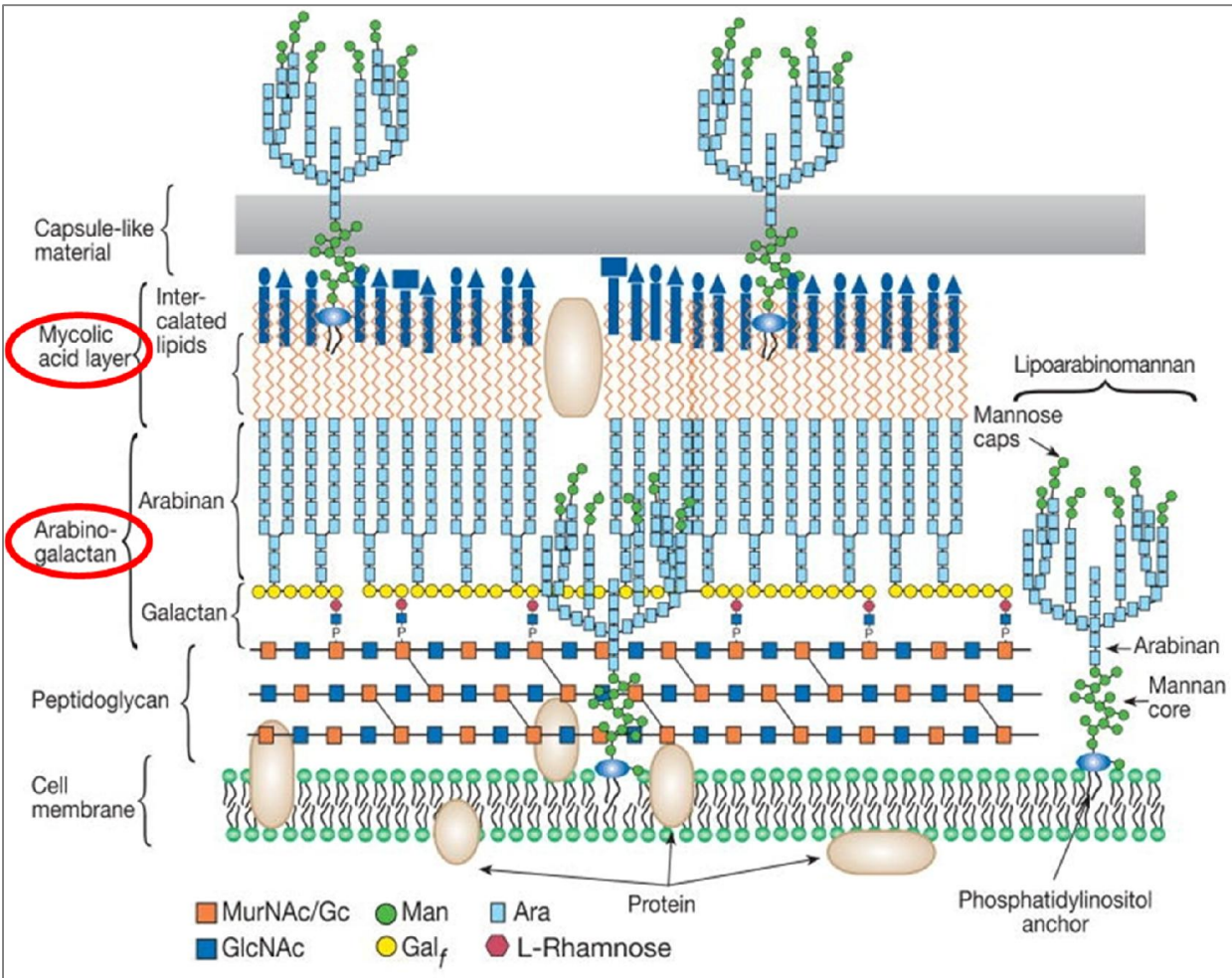


Figure 1: Cell wall structure of *Mycobacterium tuberculosis*.
 (Adapted from <http://2009.igem.org/Team:SupBiotech-Paris/Concept1>)

The capsule-like layer contains proteins, carbohydrates, and lipids forming the unique mycolyl-arabinogalactan-peptidoglycan complex of the cell wall. These surface structures tend to shed and/or cleave upon contact with the host cells. The surface of *M. tuberculosis* is rich in mannose-derived molecules such as mannan, mannose-capped lipoarabinomannan, lipomannan, arabinomannan, phosphatidyl-myoinositol mannosides, and mannoglycoproteins. The molecules facing the exterior of the cell surface act as ligands for alveolar macrophages receptors (Torreles et al., 2010). Furthermore, this lipid-rich shield effectively decreases

permeation of therapeutic agents, which significantly contributes to the difficulty of eradicating mycobacterial infections.

Although *M. tuberculosis* can infect any tissue in the body, the lungs represent the main route of pathogen entry and are the sites of most common disease manifestation. TB spreads through microorganism-containing droplets that are expelled by patients suffering from active disease while coughing.

According to the statistics compiled by the World Health Organization (WHO), less than 10% of infected patients will develop active disease during their lifetime. However, in the absence of appropriate treatment, 50% of these cases will be fatal. TB is more deleterious in patients with compromised immunity due to other underlying conditions, including diabetes mellitus, HIV infection, and malnourishment. In adults, reactivation of a latent infection is the major cause of developing disease symptoms. In immunocompromised individuals, newborns, and the elderly population, disease manifestations typically occur after first exposure to the bacteria (WHO, 2015).

1.1.2. Therapeutic Strategies

Conventional pharmacological approaches in tuberculosis treatment focus on drug regimens with rifampicin and isoniazid, which represent the two most important antibiotics. To reduce the possibility of drug resistance and treatment failure, they can be prescribed together with pyrazinamide and/or ethambutol. These four drugs are considered first-line treatment against TB. Clinical success of this regimen requires patients to adhere to this combination for two months, followed by additional four months of rifampicin and isoniazid (Walker et al., 2011). Isoniazid is a water-soluble anti-TB agent. It is a prodrug activated by catalase-peroxidase to

produce several therapeutically effective species, including reactive oxygen radicals such as superoxides and peroxides as well as isonicotinic acyl intermediates. These molecules target the TB enoyl-acyl carrier protein reductase, which plays a central role in the biosynthesis of mycolic acid (Shoeb et al., 1985). Rifampicin, in contrast, is a lipid- soluble antibiotic that binds to the β -subunit of bacterial RNA polymerase, thus, blocking formation of RNA chains. Pyrazinamide is also a prodrug that is converted by *M. tuberculosis* pyrazinamidase enzyme to pyrazinoic acid. This active metabolite accumulates inside the microorganism and causes acidification of the cytoplasm, which effectively reduces the cell membrane potential leading to permanent impairment of vital membrane transport function (Zhang et al., 2003). Ethambutol is a bacteriostatic drug that inhibits arabinan, arabinogalactan, and lipoarabinomannan polymerization, thus, preventing formation of the protective cell wall (Mikusova et al., 1995). A summary of the mechanisms of action of these first-line antibiotics is illustrated in Figure 2.

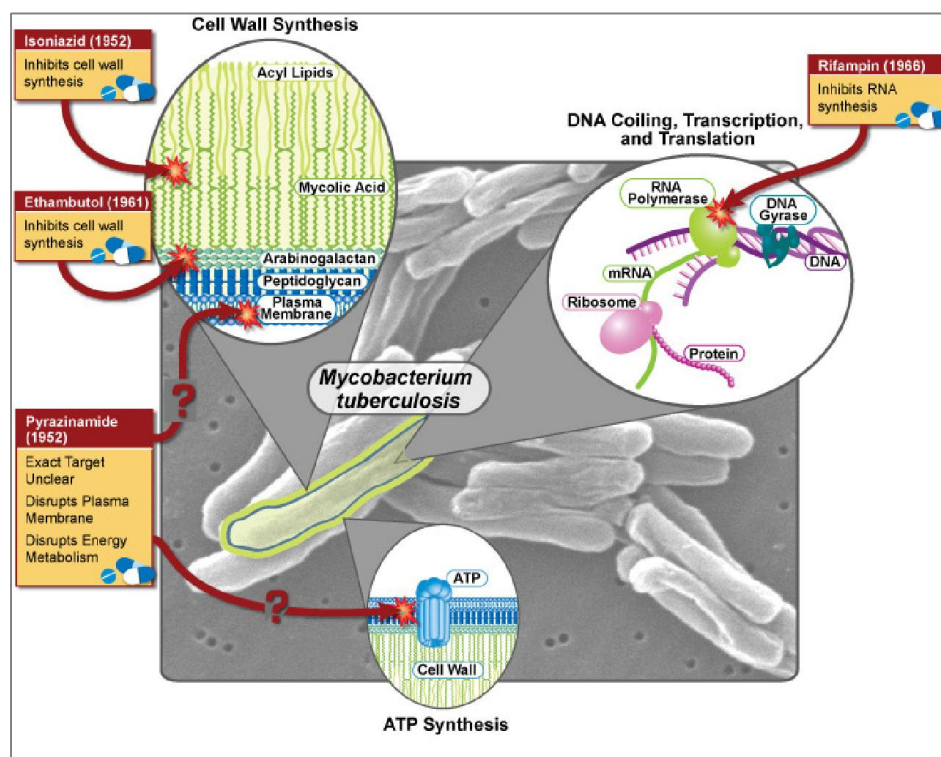


Figure 2: Mechanism of action of first-line anti-TB drugs. Adapted from the CDC.

Unfortunately, long-term administration of isoniazid, rifampicin, and pyrazinamide is associated with dose-dependent hepatotoxicity. Other serious side effects include peripheral neuropathy with isoniazid and optic neuritis with ethambutol (Walker et al., 2011). Nevertheless, these drugs are still used as first-line intervention for TB patients due to the lack of safer alternatives that results in equivalent efficacy.

Recommended treatment regimens of TB in adults and children with commercially available anti-TB dosage forms are summarized in Table 1.

Table 1: Conventional Dose Regimens of Anti-TB Drugs

Drug	Forms available	Dosage			
		Adults daily	Adults intermittent (doses per week)	Children daily	Children intermittent (doses per week)
Rifampicin	Capsules 150mg, 300mg ^b Liquid 100mg in 5 mL Injection for infusion 300mg	450mg (<50kg) 600mg (>50kg)	15 mg/kg (3)	10mg/kg	15 mg/kg (3)
Isoniazid	Tablets 50mg ^b Injection 25 mg/mL Elixir (special order) ^c	300mg	15 mg/kg (3)	5–10mg/kg	15 mg/kg (3)
Ethambutol ^f	Tablets 100 mg, 400mg ^b Mixture ^c	15 mg/kg ^d		As adult dose	30mg/kg (3)
Pyrazinamide	Tablets 500 mg	1.5 g (<50 kg) 2.0 g (≥50 kg)	2.0g ^d (<50 kg) (3) 2.5 g ^e (≥50 kg)	35 mg/kg	
Streptomycin	Injection 1 g	750mg (<50 kg) 1 g (<50kg)	750mg–1 g ^e	15 mg/kg	

^aSome of the doses quoted are not licensed but have been recommended by the British Thoracic Society.
^bAlso available as combined oral preparations.
^cMixture may be prepared extemporaneously.
^dDoses refer to patients under 50kg. Reduce by 500mg for patients weighing less than 50kg.
^eDrug levels should be monitored to prevent toxicity.
^fAcute calculation is required to reduce the risk of toxicity.

Source: Walker et al., 2011

The prolonged duration of treatment, combined with the high probability of drug-induced side effects, generally leads to poor adherence of TB-infected patients to these drug regimens. As a consequence of premature treatment interruption, chromosomal mutations in *M. tuberculosis* can occur that increase the incidence of drug-resistant tuberculosis (WHO, 2015).

Drug resistance can be divided into two categories: (1) multiple drug resistance (MDR) and (2) extensively-drug resistance (XDR). MDR is caused by bacteria that are resistant to at least isoniazid and rifampicin. Clinical cases of MDR are treated with oral and injectable second-line anti-TB drugs including aminoglycosides, fluoroquinolones, para-aminosalicylic acid, and cycloserine. Treatment must be maintained for at least 24 months, which significantly increases the financial burden on patients (Walker et al., 2011).

XDR, in contrast, refers to resistance against rifampicin, isoniazid, fluoroquinolone, and any of the second-line injectable anti-TB drugs, including amikacin and kanamycin. To date, XDR infection is considered untreatable using currently available antibiotics (WHO, 2010). However, new drug molecules such as SQ-109, PA-824 (nitroimidazoles group), and TMC 207 (diarylquinolones group) are under development that may offer viable therapeutic options for XDR patients in the future (NIH, 2015).

1.2. The Role of Alveolar Macrophages in Pulmonary Immune Defense

The respiratory epithelium exhibits several defense mechanisms against inhaled foreign materials. This includes a highly efficient mucociliary clearance as well as an active immune surveillance responding with production of several potent biochemical mediators. If microorganisms or foreign particles reach the alveolar space, alveolar macrophages, dendritic

cells, monocytes, neutrophils, and lymphocytes will act in concert to initiate an effective immune response. Alveolar macrophages (AM) constitute about 90% of the cells recovered in bronchoalveolar fluid from healthy individuals. Consequently, it is predicted that these cells represent the first-line of defense against the inhaled TB bacteria (Torrelles et al., 2010).

AMs, originally derived from blood-circulating monocytes, participate in innate immune defense by engulfing and digesting microorganisms and cellular debris via phagocytosis (Kaufmann, 2000). In addition, AMs contribute to adaptive immune defense activities by releasing biochemical signals that stimulate other immune cells such as T-lymphocytes and B-lymphocytes to take action against the invading pathogens. Several mechanisms are described by which AMs can eliminate phagocytosed pathogens. The most prominent mechanism is the activation of a biochemical cascade that leads to acidification of the phagosome containing engulfed microorganisms (see Figure 3).

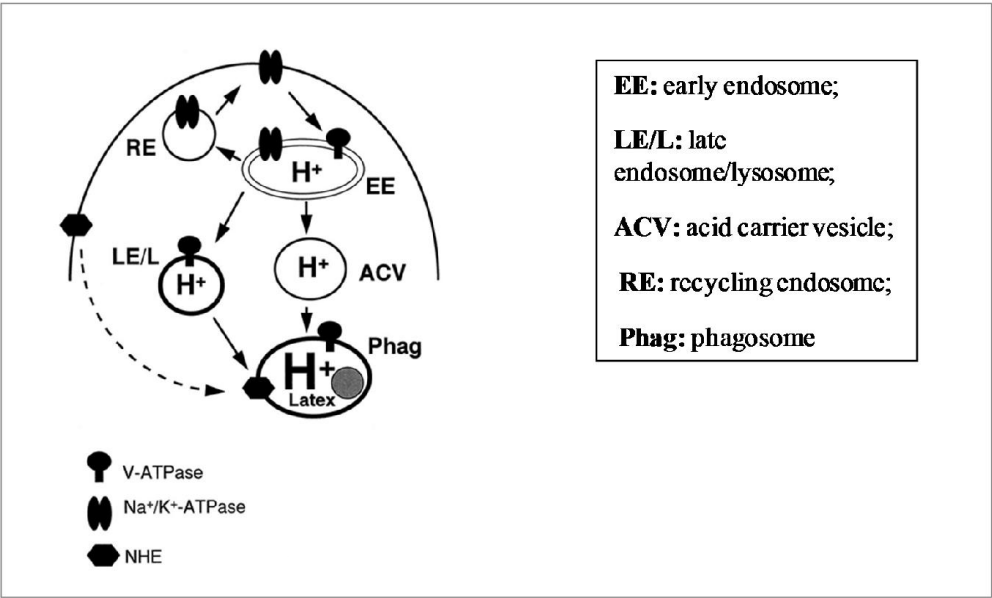


Figure 3: Biochemical pathway of phagosome acidification in macrophages. (Modified from Hackam et al., 1997).

After phagocytosis, a pathogen is sequestered within the phagosome, which is an intracellular vesicle derived from the plasma membrane. To facilitate enzyme-mediated digestion, the phagosome lumen is acidified by the action of cellular enzymes, including the Na^+/K^+ -ATPase, vacuolar type H^+ -ATPases (V-ATPases), and the Na^+/H^+ exchanger (NHE) (Hackam et al., 1997). The Na^+/K^+ -ATPase drives an inward Na^+ gradient with an outward movement of K^+ ions from the cell. Since the NHE is usually localized in the cellular membrane of macrophages, phagosome formation by invagination of the cell membrane assumes the presence of this critical antiporter in the phagosome. The NHE facilitates exchange of one intracellular Na^+ ion for one extracellular H^+ ion, thus, decreasing the pH value of the early phagosomal lumen. The V-ATPase plays a critical role in acidifying lysosomes. Together with the Na^+/K^+ -ATPase, these two enzymes transform early endosomes into acid-carrying vesicles. Lysosomes and acid-carrying vesicles fuse with the pathogen-containing phagosome, resulting in a highly acidic compartment that facilitates effective clearance of engulfed microorganisms via activation of different proteolytic enzymes, including hydrolases, superoxide dismutases, and lysozymes (Russel et al., 2005).

In addition, AMs are capable of producing a diverse array of reactive oxygen and nitrogen radicals in addition to cytokines such as $\text{IL-1}\beta$, $\text{TNF-}\alpha$, and $\text{IFN-}\gamma$ that are secreted by T-lymphocytes. The presence of these biochemical mediators stimulates production of nitric oxide from arginine, which reacts with superoxide anions to yield the strongly oxidizing peroxynitrite (Yang et al., 2009). Exposure of vesicle-entrapped bacteria to these reactive oxygen and nitrogen species denature critical bacterial biomacromolecules such as DNA, lipids and proteins, which ultimately leads to elimination of the pathogens.

1.2.1. Molecular Aspects of *M. tuberculosis* Interaction with Alveolar Macrophages

Earlier studies demonstrated that *M. tuberculosis* primarily resides in AMs of infected individuals (Bermudez et al., 1996). It is hypothesized that TB bacteria enter AMs via receptor-mediated phagocytosis. In general, AMs can recognize bacteria by two major pathways. First, binding of bacterial surface molecules and/or secreted proteins from *M. tuberculosis* to complement receptors that are expressed on the macrophage cell membrane (Schlesinger, 1993). Specifically CR1, CR3, and CR4 are predicted to play a major role in this receptor-mediated pathway (Russell, 2005). Van Crevel and colleagues reported that TB bacilli entering macrophages after CR1 binding have a greater likelihood of survival than those internalized via CR3 or CR4 (van Crevel et al., 2002). Alternatively, Fenton and co-workers described macrophage phagocytosis facilitated via mannose receptors. According to their findings, bacteria internalized via mannose receptors enter with limited ability to fuse with lysosomes (Kang et al., 2005). This may explain why some TB strains are considered more virulent when entering macrophages via the mannose receptor pathway.

Since *M. tuberculosis* has the ability to interfere with different macrophage-specific clearance mechanisms, engulfed bacilli may survive inside macrophages for a prolonged time period. Cytokines released from CD4⁺, CD8⁺ and $\gamma\delta^+$ T-lymphocytes stimulate infected macrophages, which results in formation of granulomatous structures in the lungs. Within those granulomas, virulent TB bacilli remain protected from pulmonary clearance mechanisms and adopt for intracellular residence within those lesions. This results in TB patients carrying the pathogen without developing disease symptoms. In situations where the immune system of such individuals is suppressed, *M. tuberculosis* actively initiates replication inside those granulomas. Subsequently, this leads to formation of caseous detritus, a product of cellular destruction in

the center of the granulomatous lesion characterized by a high lipid content. Caeseous detritus serves as an important source of nutrients for these bacteria, which further augments bacterial replication. Finally, disintegration and liquefaction of this mass can spread pathogenic microbes, and as soon as the cavitation approaches the alveoli, patients become infectious (Kaufmann, 2000).

1.2.2. Interference of *M. tuberculosis* with Alveolar Macrophages Clearance

Various studies identified different mechanisms by which *M. tuberculosis* can evade macrophage-associated clearance mechanism.

a) Inhibition of phagosome–lysosome fusion

Phagosome–lysosome fusion is essential for eliminating intracellular pathogens because lysosomal proteolytic enzymes and acidic contents are delivered to the phagosomes during this process. *M. tuberculosis* has the ability to prevent phagosome–lysosome fusion by secreting sulfatides and polyanionic trehalose glycolipids that are not only components of bacterial virulence but also bind to lysosomal membranes rendering them non-fusible (Moulder, 1985). Sulfatides and polyanionic trehalose glycolipids secreted by *M. tuberculosis* are taken up by lysosomes, limiting their movement and, hence, reducing the frequency of phagosome–lysosome collisions. Furthermore, Ferrari and co-workers demonstrated that retention of tryptophan aspartate–containing coat (TACO) on phagosomes by living mycobacteria also prevents cargo delivery of lysosomes to the pathogen-containing phagosomes. TACO is a protein present on the surface of phagosomes-containing viable mycobacteria. This protein is usually released before phagosomal fusion with lysosomes. In TACO-deprived macrophages,

mycobacteria were readily transported to lysosomes followed by effective degradation. The presence of TACO in mycobacteria-infected macrophages prevented delivery of lysosomes and, consequently, prolonged intracellular survival of the pathogen (Ferrari et al., 1999).

b) Inhibition of phagosomal acidification

Mycobacteria synthesize protein tyrosine phosphatase A (PtpA) that enables exclusion of the V-ATPase in phagosomes (see Figure 3, Wong et al., 2011). Upon internalization of *M. tuberculosis*, secreted PtpA will dephosphorylate and eventually inactivate VPS33B, a macrophage regulatory membrane protein that is necessary for phagosome-lysosome fusion. This will prevent transfer of the V-ATPase to phagosomes. As a result, the lumen of Mycobacteria-containing phagosome is less acidic (i.e., pH value around 6.2 instead of pH 4.7-5.5) limiting effective pathogen clearance by the acid-dependent enzymes. (Sturgill-Koszycki et al., 1993).

c) Protection against oxidative radicals

M. tuberculosis can secrete enzymes capable of inactivating free radicals that are produced by macrophages to oxidize invading pathogens. This includes enzymes such as the alkyl hydroperoxide reductase subunit C, which facilitates neutralization of peroxynitrite (Bryk et al., 2002) and the methionine sulfoxide reductase, which dissociates peroxynitrite-modified methionine residues (St John et al., 2001). In addition, Yuan and co-workers described earlier that *M. tuberculosis* has the ability to chemically modify its mycolic acids by cyclopropanation. As a consequence of this cis-cyclopropane modification, these slow-growing bacteria will be protected from oxidative stress (Yuan et al., 1995).

In summary, *M. tuberculosis* creates a “safe” environment inside AMs mainly by manipulating biochemical mechanisms essential for acidification of pathogen-containing phagosomes. This unique feature of TB-infected macrophages constitutes the scientific basis for designing selective drug delivery systems intended to preferential release of a therapeutic payload in TB-infected macrophages.

1.3. Drug Delivery Technology to Manage Tuberculosis

1.3.1. Conventional Drug Delivery Systems used in TB

To date, commercially available delivery systems of anti-TB agents are limited to oral and parenteral routes of administration using compressed tablets, capsules, or solutions. As a consequence, drug distribution is non-specific leading to severe side effects. Combined with the prolonged duration of treatment that is required for achieving a sustained therapeutic response in infected individuals, a significant fraction of TB patients on conventional drug regimens becomes non-compliant, which aids in the development of MDR. As parenteral administration of anti-TB formulations causes pain and discomfort, it is not considered a viable alternative for long-term therapy of TB (Du Toit et al., 2006). Furthermore, unfavorable pharmacokinetic properties of anti-TB drugs taken orally that result in highly variable plasma concentrations negatively affect patient compliance. Hereditary differences in acetylation status increase the risk of hepatotoxicity for slow acetylators who are taking INH orally (Huang et al., 2002). Long-term administration of rifampicin has been demonstrated to induce expression of cytochrome P450 metabolizing enzymes, which can decrease oral bioavailability of concomitantly administered drugs (Baciewicz et al., 1984). To overcome the predicament of

poor patient compliance associated with conventional drug delivery systems of anti-TB drugs that increases the risk of MDR, alternate routes of administration as well as improved drug delivery technologies that can achieve selective targeting of TB-infected AMs must be explored.

1.3.2. SMART Drug Delivery Systems

Utilization of pharmaceutically acceptable excipients that can alter physicochemical properties in response to external or internal stimuli offers a novel avenue in drug delivery to overcome significant limitations associated with conventional dosage forms. For TB patients, nonadherence to long-term treatment and poor clinical outcome can be improved by reducing the dose frequency using sustained or controlled drug delivery systems. Selective targeting of TB-infected tissues, specifically pulmonary AMs, will further increase patient compliance due to anticipated reduction in drug-induced side effects (Bullo et al., 2012). Consequently, this research attempts to create Systems to Maximize Access, Retention, and Therapy or Systems to Mute until Activation by a Remote Trigger (SMART) drug delivery systems for TB patients that can be administered via inhalation for selective targeting of pulmonary AMs.

Historically, various polymers have been designed that change their physicochemical properties in response to different stimuli (Bennet et al., 2014). These stimuli are summarized in Table 2.

Table 2: Overview of Stimuli-Induced SMART Drug Delivery Systems.

Stimulus	Example	Reference
Chemical	pH	Foss et al., 2004
	Gases (hypoxia)	Thambi et al., 2014
	Redox reactions	Meng et al., 2009
Biochemical	Enzymes	De La Rica et al., 2012
	Hormones	Chung et al., 2013
Physical	Electric field	Kwon et al., 1991
	Magnetic field	Allam et al., 2013
	Optical (laser)	Xiong et al., 2013
Multi-stimuli	Temperature/pH/redox	Klaikherd et al., 2009

In cancer therapy, for example, thermosensitive polymers allow fabrication of stimulus-responsive drug delivery systems where drug release is facilitated by gel-sol transition at a critical solution temperature (Abulateefeh et al., 2011). Since the tumor microenvironment is approximately 1–2°C warmer than normal healthy tissue (Vaupel et al., 1989), thermos-responsive polymers preferentially dissolve and release the drug at the tumor site sparing healthy tissue from drug exposure, which effectively reduces side effects (Rejinold et al., 2011).

For oral drug delivery, pH-responsive polymers have been used for decades to prevent premature drug release under acidic conditions of the stomach (Foss et al., 2004). Suitable pH-responsive polymers contain ionizable groups attached to the backbone of the molecule. In response to changes in environmental pH, the coiled polymer chains expand due to electrostatic repulsion from the charges generated by ionization. This conformational change triggers release of encapsulated payload in response to an external pH stimulus.

Polymerization products of acrylic or methacrylic acid, including corresponding esters such as Eudragit™ are examples of pH-responsive polymers which have been widely used by pharmaceutical industry to prepare enteric coated and/or controlled release drug delivery systems (Evonik, 2015). Selection of defined functional groups in the side chain of this polymer allows precise tuning of release properties under desired pH conditions. Different pH-dependent dissolution profiles of commercially available Eudragit™ polymers are summarized in Figure 4.

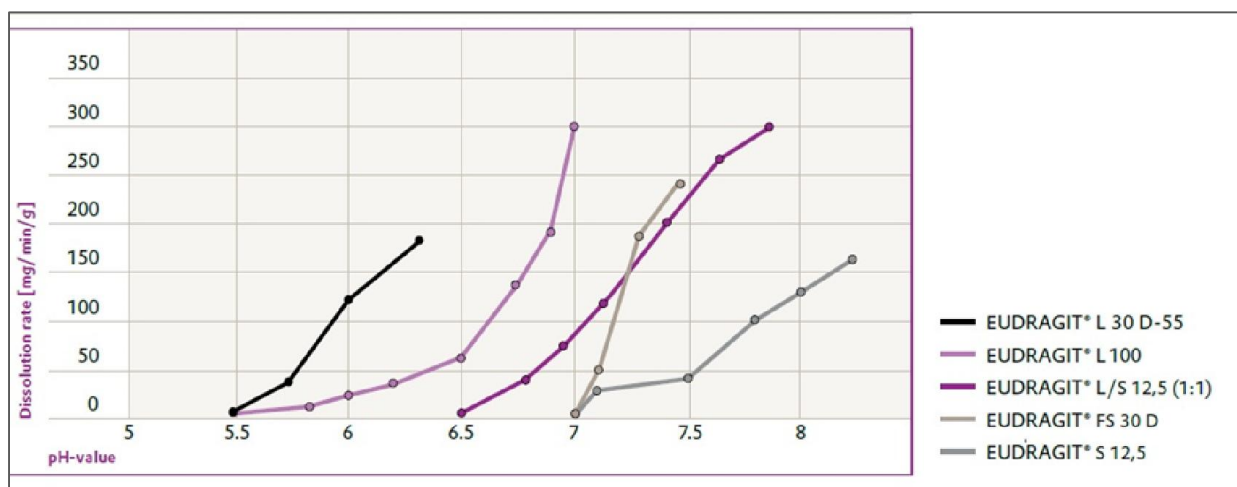


Figure 4: pH-dependent dissolution rates of Eudragit polymers. (Source: <http://eudragit.evonik.com>)

Khan and co-workers used Eudragit L100 and Eudragit S100 to coat mesalazine tablets for pH-dependent colon-targeted oral drug delivery (Khan et al., 2000). Eudragit L-100 preferentially dissolves at pH values greater than pH 6.0, while Eudragit S-100 only starts to dissolve at pH >7.0. The results from this study demonstrate that these two polymers can be used to prepare oral formulations capable of selectively releasing mesalazine at any desirable region of the intestine in response to luminal pH between 6.0 and 7.0.

Colloidal particles with diameter of less than one micrometer have been utilized as efficient delivery tools for therapeutic molecules (NIH, 2012). These nanoparticles (NPs) can be fabricated using a diverse array of materials isolated from natural sources such as alginate, chitosan, and albumin or prepared by chemical synthesis, including polyacrylamides, polycaprolactones, poly lactide-co-glycolide, or solid lipids (Gelperina et al., 2005).

Depending on the matrix composition and fabrication design, NPs can be categorized into (1) monolithic nanoparticles (or nanospheres) in which the payload is dispersed in the polymeric matrix and (2) nanocapsules in which the payload is confined within a hydrophobic or hydrophilic core surrounded by a shell-like membrane (Kreuter 2004).

NP represents a versatile drug delivery platform for incorporation of hydrophobic and hydrophilic substances that may enhance the stability of these payloads. In addition, NPs offer high encapsulation capacity and can be administered by various routes of administration (Gelperina et al., 2005). Most relevant to this research, NPs have been demonstrated to accumulate in AMs, the reservoir for *M. tuberculosis* bacilli (Gupta et al., 2012). Anisimova and co-workers explored encapsulation of isoniazid and streptomycin into poly (butyl cyanoacrylate) NPs. Intracellular accumulation of both drugs encapsulated in NPs was greater in human blood monocytes when compared to non-encapsulated drugs formulations and resulted in significantly improved antimicrobial activity against *M. tuberculosis* inside human monocytes-derived macrophages (Anisimova et al., 2000). Similarly, Fawaz and colleagues demonstrated improved pharmacological activity of intravenous ciprofloxacin encapsulated in poly (isobutylcyanoacrylate) NPs against TB bacteria inside infected macrophages when compared to an equivalent intravenous drug dose (Fawaz et al., 1998).

NPs specifically offer promising opportunities for pulmonary administration of anti-TB drugs. In addition to preferential uptake by AMs, inhaled drug-loaded NPs bypass extensive hepatic first-pass metabolism, and consequently, minimize serious adverse effects associated with anti-TB drug regimens (Bullo et al., 2012). Pandey and co-workers investigated the effect of a single dose of (poly lactide-co-glycolide)-encapsulated isoniazid, rifampicin, and pyrazinamide NPs administered in guinea pigs by nebulization (Pandey et al., 2003). Sustained therapeutic drug levels were measured in the lungs for up to 11 days. Subsequent administration of these nebulized NPs once every 10 days (total 5 doses) to TB-infected guinea pigs resulted in eradication of the bacilli in the lung. In comparison, 46 daily oral doses were required to obtain an equivalent therapeutic effect.

As particle size critically determines tissue distribution after inhalation (Labiris et al., 2003), the objective of this research project was to fabricate NPs with a defined diameter of approximately 250 nm. Inhaled particles larger than 10 μm are deposited in the oropharyngeal zone by inertial impaction. These large particles can contribute to a desired therapeutic response but only after absorption from the gastrointestinal tract. To expose AMs to drug-loaded NPs, gravitational sedimentation laws require particle diameter <500 nm. According to Labiris and co-workers, particles with diameter of approximately 250 nm exhibit a longer residence time in the alveolar region, which is predicted to allow sufficient time for resident AMs to internalize this drug-containing SMART drug delivery system.

2. Research Objective

2.1. Hypothesis

Nanoparticles fabricated from acrylic polymers facilitate stimulus-induced payload release under pH conditions present in *M. tuberculosis*-infected macrophages.

2.2. Specific Aims

To explore this hypothesis experimentally, we propose the following specific aims:

- **Specific Aim 1**

To fabricate Eudragit L-100 NPs of approximately 250 nm in diameter and explore *in vitro* payload release at pH 5.5, 6.2, and 7.4.

- **Specific Aim 2**

To assess cellular internalization efficiency and pH-dependent payload release from the Eudragit L-100 NPs in control and pH-modified macrophages.

3. Materials and Methods

3.1. Materials

Eudragit® L-100 molecular weight (M.W.) = 125,000 was a gift from Evonik Industries AG (Darmstadt, Germany). Fluorescein isothiocyanate-labelled dextran, M.W. = 40,000 (FD40) was purchased from Sigma-Aldrich (St. Louis, MO). Rhodamine123 UltraPure grade (M.W. = 380) was supplied by Anaspec Inc. (Fremont, CA). Pierce BCA Protein Assay kit was obtained from Thermo Fisher Scientific Inc. (Pittsburgh, PA). CellTiter-Glo® Luminescent Cell Viability Assay kit was obtained from Promega Corporation (Madison, WI). RIPA Lysis Buffer was purchased from Santa Cruz Biotechnology (Dallas, TX). Spectra/Por 3 dialysis membrane with M.W. cut-off = 3.5 kDa was purchased from Spectrum® Laboratories, Inc. (Rancho Dominguez, CA). All other chemical reagents were of high purity or analytical grade.

3.2. Cell Culture

The MH-S mouse alveolar macrophages cell line CRL-2019 was purchased from American Type Culture Collection (Rockville, MD). Cells were routinely maintained in phenol red-free Dulbecco's modified Eagle medium (DMEM) from Corning Cellgro (Manassas, VA) supplemented with L-glutamine 2% (v/v), non-essential amino acids 1% (v/v), penicillin/streptomycin (10,000 I.U./mL each), 2-mercaptoethanol 0.00035% (v/v), and heat-inactivated fetal bovine serum 10% (v/v) at controlled incubation conditions of 37°C, 5% CO₂ and 90% relative humidity.

3.3. Fabrication of Eudragit L-100 Nanoparticles

Nanoparticles were prepared by the nanoprecipitation method adapted from Bharathi and colleagues, 2012. Briefly, a stock solution of rhodamine123 (Rh123) was prepared in dimethyl sulfoxide (DMSO) (1.9 mg/mL) by dissolving 9.5 mg Rh123 in 5 mL of DMSO. A standard batch of a nanoparticle suspension was prepared by combining 42 μ L of the Rh123 stock solution in DMSO with 10 mL of acetone/water (97:3, v/v). Subsequently, 100 mg of Eudragit L-100 was added gradually over 5 minutes with frequent shaking of the organic solvent until the polymer dissolved and no solid particles residues were visible. Using a Pasteur pipet, this organic phase was added drop by drop over 3 minutes into 20 mL of deionized distilled water (ddH₂O) under magnetic stirring (600 rpm). This mixture was left under stirring in fume hood for 3 hours until complete evaporation of acetone was confirmed gravimetrically. At the end, this suspension of nanoparticles was purified by centrifugation for 30 minutes at 3,900 x g using a Marathon 21000R centrifuge (IEC, Needham Heights, MA). Twenty (20) mL of the supernatant was collected and then subjected to dialysis against 2 L of 0.3 μ M HCl (pH = 3.5) using a dialysis bag under magnetic stirring at 100 rpm for 2 hours in order to eliminate the fluorescent dye adsorbed on the surface of Rh123-containing NPs. The dialysate was replaced with fresh HCl solution after two hours, and the dialysis continued overnight. The NP suspension was stored at room temperature in a dark place until further use.

3.4. Physical Properties of the Nanoparticles

Particle size distribution and zeta potential of the fabricated NP were measured by dynamic laser light scattering using the Zetasizer Nano-ZS (Malvern Instruments, Worcestershire, U.K.) according to the manufacturer's instructions. All the values of particle size reported in this project refer to the equivalent hydrodynamic diameter.

For NP size measurement, 1 mL of the aqueous NP suspension was loaded into a disposable micro-cuvette, and placed inside the device. After a 2-minute equilibrium at 25°C, laser scatter was acquired at 173° Backscatter detection. Measurements of the same sample were repeated three times, and the average and standard deviation were calculated. For the zeta potential measurement, a disposable capillary cell was used, and then placed inside the machine at 25°C and equilibrated of 2 minutes.

3.5. Rhodamine123 Encapsulation Efficiency

To determine the encapsulation efficiency of Rh123 in Eudragit L-100 nanoparticles, 2 mL of the nanoparticle suspension was loaded into a Spectra/Por 3 tubing (M.W. cut-off = 3.5 kDa) that was pre-equilibrated in ddH₂O for at least 15 minutes. Polymeric nanoparticles were dissolved by exposure to 18 mL of 0.5 M NaOH under magnetic stirring (100 rpm) for 4 hours at room temperature.

0.2 mL of the polymer-free dialysate was removed for spectrophotometric fluorescence analysis at EM = 520 nm, EX = 485 nm (Polarstar Optima, BMG Labtech, Ortenberg, Germany), and Rh123 concentration was quantified using a calibration curve of Rh123 in NaOH. Encapsulation efficiency (E.E.) was calculated in percent using the following equation:

$$E.E. \% = \frac{Q_{\infty}}{M_t} * 100 \% \quad (\text{Eq. 1})$$

Where Q_{∞} = amount of encapsulated Rhodamine123 that was released from NPs into NaOH dialysate, M_t = initial amount of Rh123 used in NPs fabrication.

The amount of Eudragit L-100 that was recovered in the fabricated nanoparticles was quantified gravimetrically. Briefly, 2 mL of nanoparticles suspension was transferred into aluminum weigh dish, and left for drying at room temperature. Samples weights were recorded using XS205 DualRange Analytical Balance (Mettler-Toledo LLC, Columbus, OH) at different time points and complete evaporation of the suspension was obtained after 24 hours. Rh123 loading capacity (L.C.) of the Eudragit L-100 nanoparticles was calculated according to the following equation:

$$L.C. = \frac{Q_{\infty}}{P} \quad (\text{Eq. 2})$$

Where Q_{∞} = amount of encapsulated Rhodamine123 that was released from NPs into NaOH dialysate, P = the amount of Eudragit L-100 incorporated in the purified nanoparticles.

3.6. Rh123 Release Kinetics *In vitro*

Time-dependent release of Rh123 from Eudragit L-100 NPs was assessed at pH 5.5, 6.2, and 7.4 using phosphate buffer solutions. Five mL of the Rh123-nanoparticle suspension were loaded into hydrated Spectra/Por 3 dialysis tubes, which were placed into a 100 mL glass beaker containing 75 mL of phosphate buffer, adjusted to the desired pH value. Rh123 release experiments were performed at room temperature under magnetic stirring at 300 rpm. At

specific time points, 200 μL aliquots were removed from the dialysate, and Rh123 was quantified fluorometrically using Polarstar Optima (BMG Labtech, Ortenberg, Germany). Fresh buffer solution was used to replace the volumes removed in order to maintain sink condition. Fluorescence readings were converted to Rh123 concentrations using standard curve data of Rh123 in phosphate buffer of the corresponding pH value, and the cumulative amount of Rh123 released at each time point was calculated using the following equation:

$$Q_n = C_n \cdot V_t + \sum_{i=1}^{n-1} C_i \cdot V_s \quad (\text{Eq. 3})$$

Where Q_n = the cumulative amounts of Rh123 released at sampling interval n , C_n = concentration of Rh123 determined at n th sampling interval, V_t = Volume of the dialysis medium = 75 mL, C_i = Rh123 concentration determined at each sampling interval, V_s = sample volume removed = 0.2 mL.

These values were subsequently divided by the total amount of the dye that was encapsulated in the nanoparticles to express cumulative release kinetics of rhodamine123 in percent:

$$R_n \% = \frac{Q_n}{Q_\infty} * 100 \% \quad (\text{Eq. 4})$$

Where R_n = cumulative Rh123 release at sampling interval n , Q_n = the cumulative amounts of Rh123 released at sampling interval n , Q_∞ = amount of encapsulated Rhodamine123 in the NP batch.

In an attempt to delineate the release mechanism of Rh 123 from nanoparticles, the pH-dependent release data were fitted to various mathematical model previously reported. The release data was linearized according to the literature, and linear regression analysis was

performed. Goodness of fit was assessed based on the value of correlation coefficient (R^2) and randomness of residuals.

a) Zero-order model

This model describes passive diffusion in systems where the rate of drug release is independent of its concentration. Mathematically, the release profile follows:

$$Q_t = Q_0 + K_0 t \quad (\text{Eq. 5})$$

where Q_t = cumulative amount of Rh123 released in time t , Q_0 = the initial amount of drug in the solution (in most cases, $Q_0 = \text{zero}$), and K_0 = the zero order release constant expressed in units of concentration/time.

To study the release mechanism, data obtained from *in vitro* release studies were plotted as Q_t versus time.

b) First-order model:

In this model, the drug release rate depends on its concentration in the dosage form. It can be expressed by the equation:

$$Q_t = Q_0 * e^{-kt} \quad (\text{Eq. 6})$$

where Q_t and Q_0 as mentioned above, k = first order rate constant, and t = time. *In vitro* release data obtained were linearized by plotting log cumulative percentage of Rh123 remaining against time.

c) Higuchi model:

This model explains the release of drugs incorporated in semi-solid and/or solid matrices by diffusion. It can be expressed by:

$$Q_t = A \sqrt{D(2C - C_s)C_s t} \quad (\text{Eq. 7})$$

In which Q_t = the cumulative amounts of Rh123 released in time t per unit area A , C = the drug initial concentration, C_s = drug solubility in the matrix media, and D = the diffusion coefficient of the drug. *In vitro* release data can be plotted as Q_t versus square root of time (Silvina et al., 2002).

d) Hixson-Crowell model

This model describes drug release by dissolution from systems where a change in surface area and diameter of the particles is present. Hixson and Crowell found that the particles' regular area is proportional to the cube root of its volume. They derived the following equation:

$$Q_\infty^{1/3} - Q_t^{1/3} = \kappa * t \quad (\text{Eq. 8})$$

Q_∞ = amount of drug in the dosage form, Q_t = cumulative amounts of Rh123 released in time t , and κ = a constant incorporating the surface-volume relation. Data obtained from *in vitro* release studies can be plotted as cube root of Q_t against time (Hixon et al., 1931).

e) Baker-Lonsdale model

This model describes the release of drugs from spherical matrices, in which the release mechanism is a combination of polymer erosion and diffusion:

$$\frac{3}{2} * \left[1 - \left(1 - \frac{Q_t}{Q_\infty} \right)^{\frac{2}{3}} \right] - \frac{Q_t}{Q_\infty} = k_b t \quad (\text{Eq. 9})$$

Q_t/Q_∞ = fraction of drug released at time t , k_b = Baker-Lonsdale release rate constant. *In vitro* release data was plotted as $[d(Q_t/Q_\infty)]/dt$ against the root of time inverse (Baker et al., 1974).

f) Korsmeyer-Peppas model

Korsmeyer and Peppas derived an equation that attributed drug release to dynamic swelling and dissolution of the polymer:

$$\frac{Q_t}{Q_\infty} = a t^n \quad (\text{Eq. 10})$$

Where a = constant incorporating structural and geometric characteristics of the drug dosage form, n = the release exponent, t = time. *In vitro* release data were plotted as $\log Q_t$ versus \log time (Korsmeyer et al., 1983).

3.7. Cells Viability

MH-S macrophages were seeded in 96-well plate at density of 50,000 cells/well and incubated in 200 μ L serum-containing DMEM for 48 hour at 5% CO₂ (v/v), 37° C. Then, culture medium

was removed by aspiration, and cells washed twice with pre-warmed phosphate buffer saline pH 7.4 (PBS). 100 μ L of NPs equivalent to a polymer concentrations range from 0.93 to 4.65 mg/mL were added to the cells and incubated at 37° C for up to 6 hours. At the end of each incubation period, NP suspension was removed by aspiration and cells were washed once with ice-cold PBS. Thereafter, 100 μ L serum-containing DMEM was added to each well and incubated overnight at 5% CO₂ (v/v), 37° C. The next day, 100 μ L/well of the CellTiter Glo reagent was added, and the plate was mixed for 2 minutes using an orbital shaker. After a rest for 10 minutes at room temperature, luminescence was quantified using the Polarstar Optima microplate reader. The cells that were exposed to different concentrations of Eudragit L-100 gave luminescence readings that were normalized to those of the cells that were incubated with the negative control (serum-free DMEM) to estimate the percentage of cell viability. RIPA buffer (30 μ L/well) which resulted in complete cellular lysis was considered as positive control. Results were fitted to the sigmoidal dose-response Eq. 11 using GraphPad Prism 5.0

$$\text{Cell viability} = \frac{100}{1 + 10^{(\log IC_{50} - x) \cdot HillSlope}} \quad (\text{Eq. 11})$$

where x = polymer concentration (mg/mL), IC_{50} = polymer concentration that compromise the growth of 50 % of the cells. *HillSlope* describes the steepness of the curve.

3.8. Cellular Uptake Studies

MH-S cells were seeded in 96-well transparent plate at a density of 50,000 cells/well and incubated for 48 hours in serum-containing phenol red-free DMEM. Prior to uptake experiments, cells were washed twice with 200 μ L of PBS at room temperature and 200 μ L/well

of the nanoparticle suspension was added. Control experiments were performed with equivalent concentration of Rh123 solution in the same medium. The cells were incubated for 30 minutes in the incubator under 5% (v/v) CO₂, 37°C. After that, the treatment was removed by aspiration and cells washed twice using ice-cold PBS. Then, 200 µL/well PBS was added, and the samples were taken for fluorescence analysis. PBS was removed from cells, and 200 µL/well RIPA lysis buffer was added. The fluorescence was measured after 1, 3, 6, and 18 hours of RIPA addition using a spectrophotometer.

3.9. BCA Cellular Protein Quantification Assay

Protein concentrations were determined using the BCA Protein Assay kit, which was prepared following the manufacturer's protocol. MH-S mouse alveolar macrophages were seeded in DMEM into transparent 96-well plate at a density of 10,000, 25,000, and 50,000 cells/well, and were divided into two groups: the control in which the cells were not subjected to washing or other manipulation steps; and the second group of cells that were subjected to these manipulations. Both groups were incubated for different periods (overnight, 24 hours, and 48 hours). At the end of each incubation period, DMEM was removed from cells of the second group, and 100 µL/well of serum-free DMEM was added. The plate was incubated for an additional 4 hours. After that, serum-free medium was removed, and the cells were washed three times with ice-cold PBS. 100 µL/well of DMEM medium was added, and the plate was incubated overnight at 5% CO₂ (v/v), 37°C. The next day, DMEM medium was removed from both groups, and 30 µL/well of RIPA lysis buffer was added. The plate was incubated for 30 minutes.

Next, 250 μL /well of BCA reagent was added to all cells, and the plate was incubated in a water bath at 37° C for 30 minutes to stabilize the signal. Absorbance was measured at $\lambda = 570$ nm using SpectraMax Plus 384 microplate reader (Molecular Devices LLC., Sunnyvale, CA), and absorbance values were converted to protein concentrations using a calibration curve prepared with bovine serum albumin standards ranging from 0 – 16 $\mu\text{g}/\text{mL}$.

3.10. Lysosomal pH

FD40 was used to measure the pH of cellular lysosomes as was adopted by Ohkuma et al. (1978) and Geisow et al. (1981).

Aliquots of 1 $\mu\text{g}/\text{mL}$ of FD40 in PBS of different pH values (3.5 – 8.5) were prepared. The fluorescence was recorded at 520 nm emission wavelength after using 485 nm and then 460 nm excitation wavelengths. The fluorescence ratio at each pH value was calculated, and a calibration curve was constructed.

MH-S cells were seeded in 96-well plate at density of 5×10^4 cells/well, and incubated in 100 μL /well of serum-containing DMEM for 24 hours at 5% CO_2 (v/v), 37° C. The next day, 100 μL /well of FD40 (concentrations equal to 0.5, 1 or 2 mg/mL in serum-free DMEM) was added, and the cells were incubated again for different periods (up to 24 hours). At the end of each period, 30 μL /well of Trypan blue (1.2 mg/mL) was added to each well. Then, FD40 fluorescence was measured at specific time intervals using excitation wavelength at 485 nm and 460 nm, and emission of 520 nm.

3.11. Simulated Lysosomal Conditions of TB-infected Alveolar Macrophages

Cells were seeded in 96 well plate at density (5×10^4 cells/well) and incubated for 48 hours at 5% CO₂ (v/v), 37° C. At the end of 48 hours, 40 µL of FD40/PBS (concentration 2.5 mg/mL) was added to each well, and the cells were incubated for 3 hours. At the end of 3 hour, cell medium and FD40/PBS mixture were removed, and cells were washed twice with ice-cold PBS. Then, 200 µL of either NH₄Cl (ranging from 0.1 – 1 mM) in amino acid-free DMEM medium (Treated cells) or the Control cells (given only amino acid-free DMEM medium) was added to each well, and the plate was incubated for 1 hour. After that, these solutions were removed, and 200 µL/well of either Rh123-loaded NPs (polymer concentration equals to 1.62 mg/mL) or the equivalent concentration of Rh123 solution in phenol red-free SFM was added to cells, and incubated for 30 minutes. The Rh123-loaded NP and Rh123 solution were removed, and cells were washed twice with ice-cold PBS. Then, 200 µL/well of PBS was added, and the samples were taken for fluorescence and confocal microscope (Zeiss LSM510 META) measurements. PBS was removed from cells, and 200 µL/well of RIPA lysis buffer was added to them. The fluorescence was measured after 1, 3, 6, and 18 hours of RIPA addition using spectrophotometer.

3.12. Confocal Microscope

The uptake of Rh123-NPs and Rh123 solution was determined by visualizing the green fluorescence inside MH-S cells using the Zeiss LSM510 Confocal Microscope (Zeiss, Germany). The LSM 510 consists of a Zeiss Axiovert 200M microscope Meta detector head (range 410-750 nm). For green fluorescence, Argon Laser was used (EX = 488 nm and EM 505-530 nm). MH-S cells were seeded in culturewell 16-chambered coverglass (Grace Bio-Labs,

Bend, OR). DMEM was removed from cells and PBS added prior to confocal microscope analysis.

3.13. Statistical Analysis

The experiments were conducted in triplicate unless otherwise stated. All results are represented in mean \pm standard deviation (SD). Statistical differences between groups were assessed for significance by GraphPad Prism 5.0 (GraphPad Software, Inc., La Jolla, CA) using analysis of variance (ANOVA) or Student's t-test. Microsoft Office Excel 2013 was used for regression analysis of *in vitro* release studies.

4. Results

4.1. Eudragit L-100 Nanoparticles

4.1.1. Physicochemical Properties of Eudragit L-100 Nanoparticles

The main objective of the NP fabrication process was to obtain colloids with an average diameter of approximately 250 nm to facilitate efficient phagocytosis by the AMs. As described by Devarajan and co-workers, factors such as polymer feed and stirring time most dramatically affect nanoparticle size (Devarajan et al., 2007).

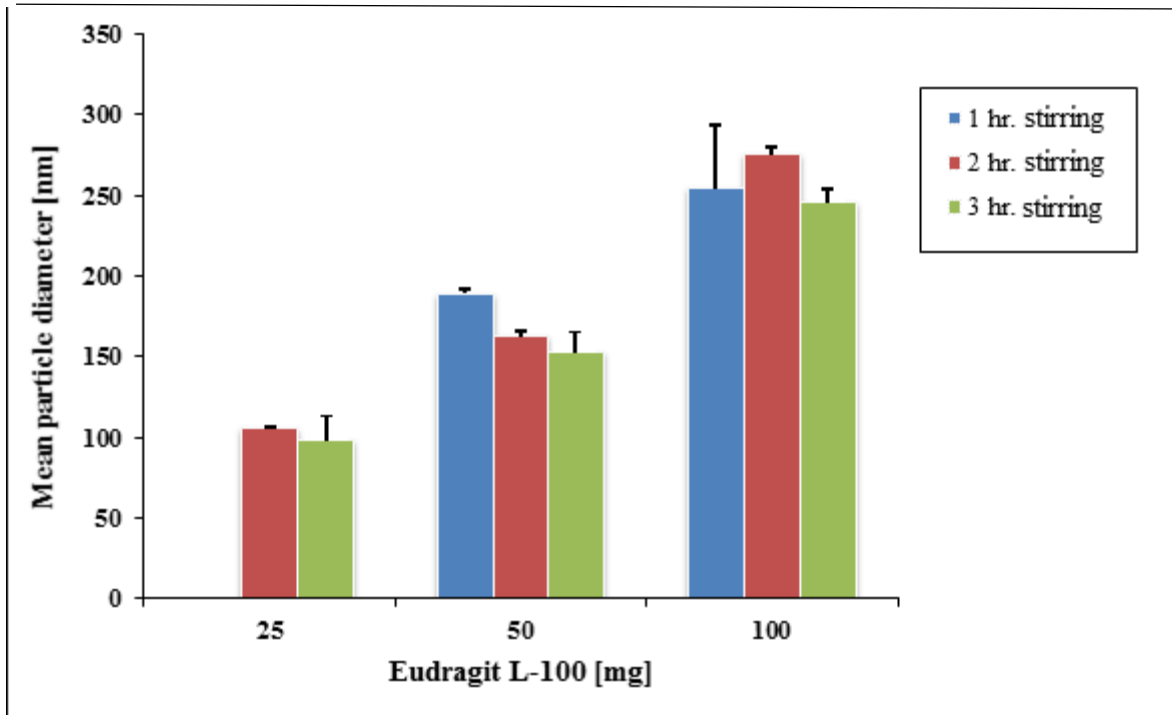


Figure 5: Optimization of NP size. Effects of magnetic stirring duration and Eudragit L-100 feed were varied during fabrication process. Mean hydrodynamic particle diameter of colloid dispersion in water was measured by DLS. Results are shown as mean \pm SD (n = 3).

The results summarized in Figure 5 demonstrated that the particle size increased with increasing polymer feed up to 100 mg of Eudragit L-100. Interestingly, stirring times between 1-3 hours

after addition of the polymer solution did not affect mean particle size if polymer feed was kept constant ($p = 0.71$ in 25 mg polymer feed; $p = 0.12$ in 50 mg polymer feed; and $p = 0.6$ for 100 mg polymer feed). Based on these results, 100 mg of Eudragit L-100 in combination with a 3 hours magnetic stirring period were selected for standard NP batch fabrication. The longer stirring time assured quantitative evaporation of acetone, which was used to dissolve the polymer. Eudragit L-100 nanoparticles prepared by this optimized nanoprecipitation technique exhibited a mean particle diameter of 270 ± 17 nm and a zeta potential of -21.8 ± 1.4 mV ($n = 3$ batches).

4.1.2. Rhodamine123 Encapsulation Efficiency

Quantifying the NP encapsulation efficiency for the drug surrogate Rh123 is essential to determine the payload capacity that is carried by these NPs and, subsequently delivered to the lysosomes of TB-infected AMs. Analytically, this is accomplished by complete dissolution of Rh123-containing NPs using an appropriate solvent followed by spectrophotometric determination of the total Rh123 concentration in solution. In an effort to achieve complete NP dissolution with a limited time frame, the effect of multiple mixing techniques, including high-shear mixing, ultrasonication, and magnetic stirring, on the size distribution of Eudragit L-100 NPs was tested. Magnetic stirring for up to 2 hours did not significantly reduce the fraction of particles $\geq 1 \mu\text{m}$, which were assumed to represent aggregates of fabricated NPs. High-shear mixing, in contrast, appeared to increase aggregations of NPs resulting in a greater fraction of particles with a diameter $\geq 1 \mu\text{m}$ (see Figure 6). Similarly, ultrasonication resulted in the formation of very large aggregates (data are not shown).

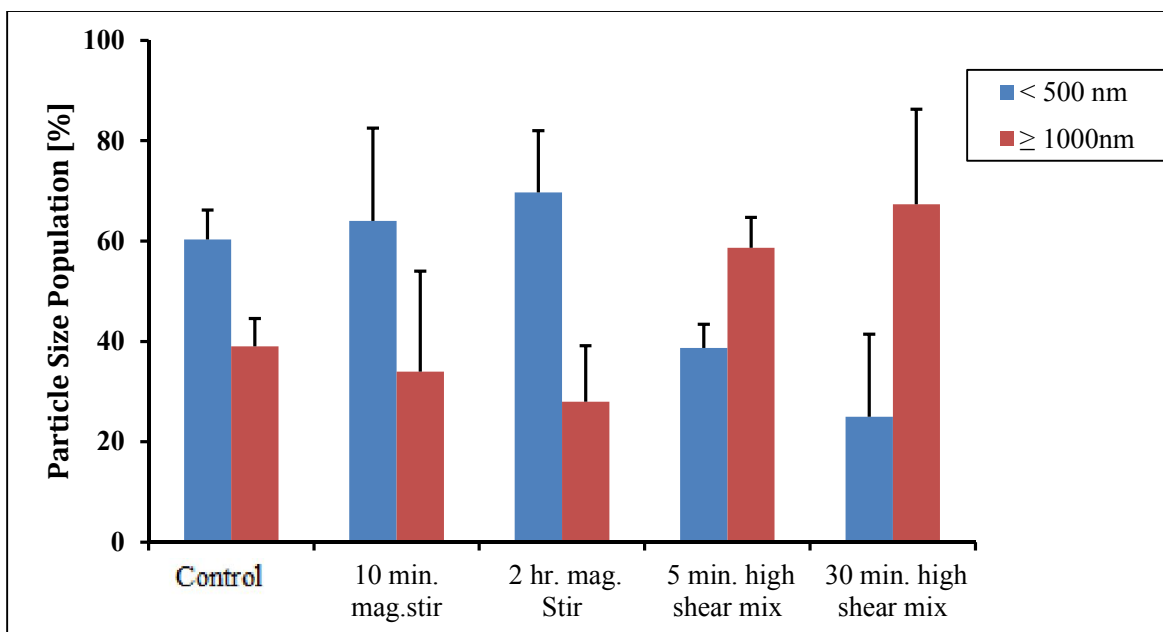


Figure 6: Effect of different mixing techniques on NP size distribution. Eudragit L-100 particle size distribution was measured by DLS after dispersion of NPs in acetone/water (97:3, v/v). Control experiments were performed with Eudragit L-100 NP under similar conditions but without application of any physical mixing. Results are shown as mean \pm SD (n = 3).

From these data, it was concluded that exposure of NPs in acetone/water to greater physical forces favors particles aggregation rather than dissolution. Therefore, different solvent systems, including 100% (v/v) of isopropanol, ethanol and acetone, were explored using magnetic stirring. Consistently, particle size measurements revealed again the presence of a significant fraction of Eudragit L-100 NPs with a diameter $\geq 1 \mu\text{m}$ when compared to control polymer dissolved in acetone/water (Figure 7).

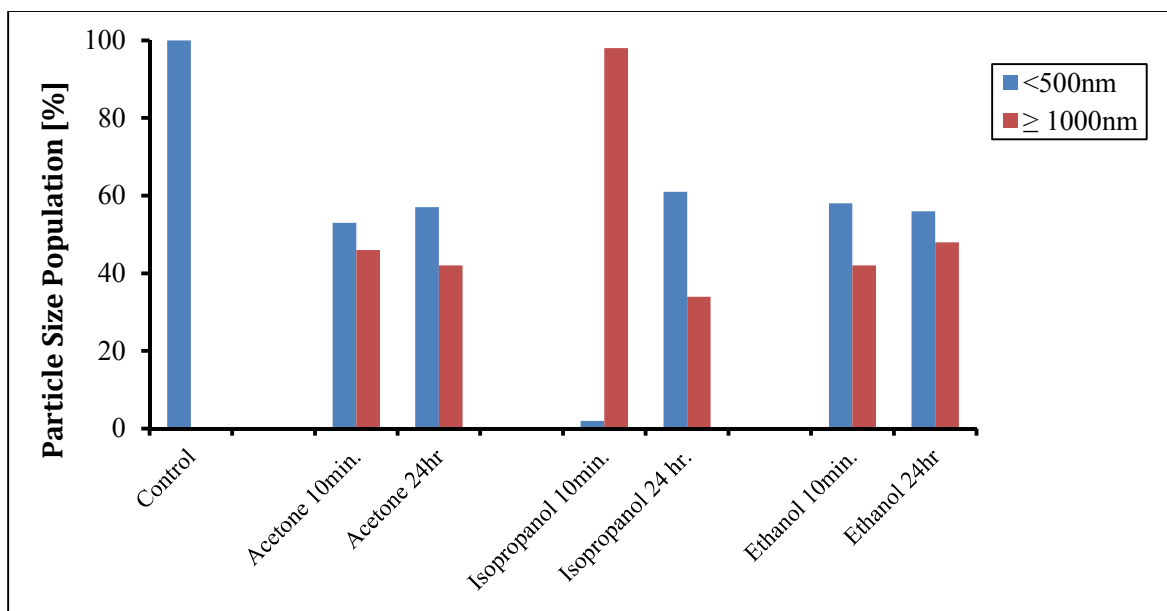


Figure 7: Effect of different solvents on NP size distribution. Eudragit L-100 NP suspension prepared in indicated solvents and incubated for 10 minutes or 24 hours under consistent magnetic stirring. Control experiments were performed using Eudragit L-100 polymer in acetone/water (97:3, v/v). Particle size distribution was measured by DLS.

The results from experiments performed with these organic solvents did not suggest sufficient success in dissolving the NPs, which is a prerequisite for accurate determination of the encapsulation efficiency. As an alternative option, sodium hydroxide solutions were investigated, which can chemically hydrolyze the ester bonds between copolymer chains (Evonik 2015).

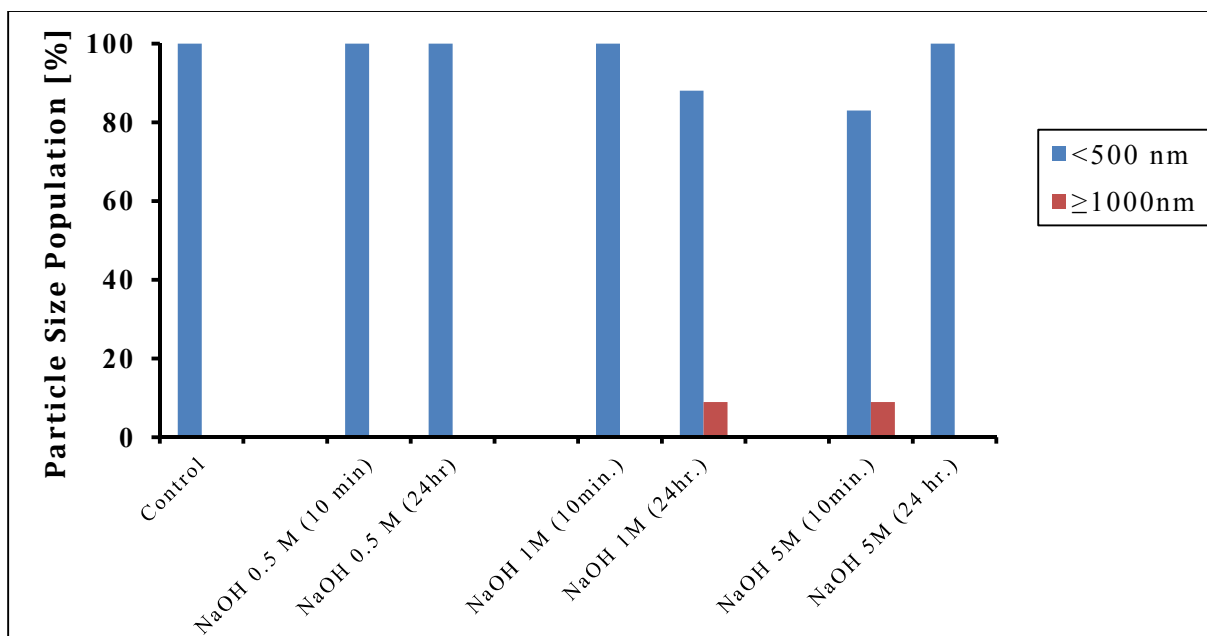


Figure 8: Effect of sodium hydroxide on Eudragit L-100 NP particle size distribution.

NPs were incubated for 10 minutes or 24 hours with aqueous NaOH solutions under magnetic stirring. Control experiments were performed using Eudragit L-100 polymer in acetone/water (97:3, v/v). Particle size distribution was measured by DLS.

Short-term incubation of Eudragit L-100 NPs in NaOH solutions ranging from 0.5-5 M consistently eliminated the fraction of aggregates $\geq 1 \mu\text{m}$ (see Figure 8). To limit possible chemical degradation of encapsulated Rh123, a 10-minute incubation of NPs in 0.5 M NaOH was selected for quantitative assessment of Rh123 encapsulation efficiency.

Since Eudragit L-100 was interfering in the spectrophotometric quantification of Rh123 (data not shown), it was necessary to separate this polymer from Rh123 by dialysis. To determine the time required for complete dissolution of Rh123-containing Eudragit L-100 NPs in 0.5 M NaOH and subsequent diffusion of released Rh123 across the 3.5 kDa dialysis membrane, dialysate samples were removed at different time points and quantified for Rh123 using fluorescence spectrophotometry. The kinetics profile of Rh123 in the dialysate is shown in Figure 9.

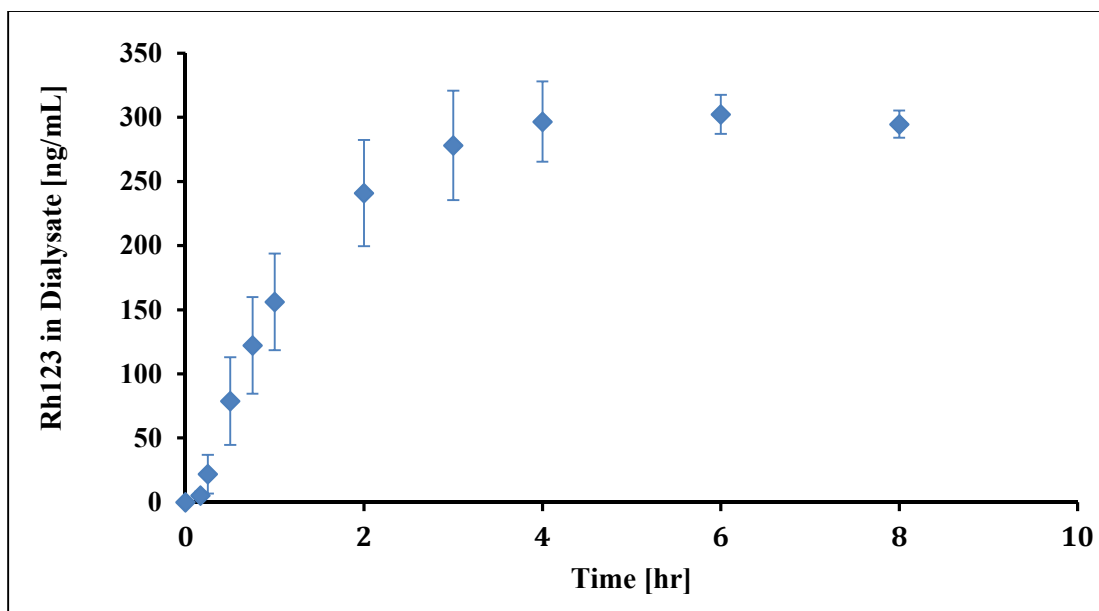


Figure 9: Dissolution of Rh123-containing Eudragit L-100 NPs kinetics. NPs suspension was incubated in 0.5 M NaOH inside a 3.5 kDa dialysis bag, and dialysate was quantified spectrofluorometrically for Rh123 using EX = 485 nm and EM = 520 nm. Results are shown as mean \pm SD. (n = 3).

Within the first few hours, increasing Rh123 concentrations were measured in the dialysate. However, the appearance rate of this fluorescent probe in the dialysate significantly decreased after 2 hours reaching equilibrium after approximately 4 hours. The results from this experiment implied that complete dissolution of the Rh13-containing Eudragit L-100 NP in 0.5 M NaOH and subsequent diffusion of the fluorescent probe across the dialysis membrane was completed after approximately 4 hours. Consequently, this time point was considered appropriate to determine encapsulation efficiency of Rh123 in Eudragit L-100 NPs.

Using six different NP batches, the mean encapsulation efficiency of Rh123 was 74 ± 2 % (w/w). To estimate the corresponding loading efficiency, the polymer amount recovered after NP purification was determined gravimetrically (= 93 % of initial Eudragit feed). Accordingly,

the loading capacity of Rh123 in the fabricated NPs was calculated as 0.63 ± 0.02 mg Rh123/mg Eudragit L-100.

To explain the effect of Rh123 incorporation and subsequent dialysis of Rh123-containing NPs on physicochemical properties of fabricated NPs, mean particle size and zeta potential were compared with Eudragit L-100 alone.

Table 3: Physical Characteristics of Eudragit L-100 Nanoparticles

	Blank Eudragit L-100 NP (n = 3)	Rh123-loaded NP (no dialysis) (n = 6)	Rh123-loaded NPs (dialyzed) (n = 3)
Nanoparticles diameter [nm]	270 ± 17	276 ± 30	238 ± 22
Zeta potential [mV]	-21.8 ± 1.4	-25.0 ± 3.0	-33.1 ± 7.1

* Values represent mean \pm SD.

As shown in Table 3, it appears that neither incorporation of Rh123 nor the use of dialysis to remove particle-adsorbed Rh123 significantly alter relevant particles properties that govern colloidal stability and cellular uptake.

4.1.3. Release Kinetics of Rh123 from Eudragit L-100 NP

The aim of this experiment was to measure the release of Rh123 from Eudragit L-100 NPs under pH conditions present in the lysosome of TB-infected phagosomes, control non-infected AMs, as well as the bronchial lumen where NPs were expected to be deposited after pulmonary administration. The cumulative release profiles of Rh123 from Eudragit L-100 NPs at pH 5.5, 6.2, and 7.4 were measured *in vitro* at 25°C using PBS.

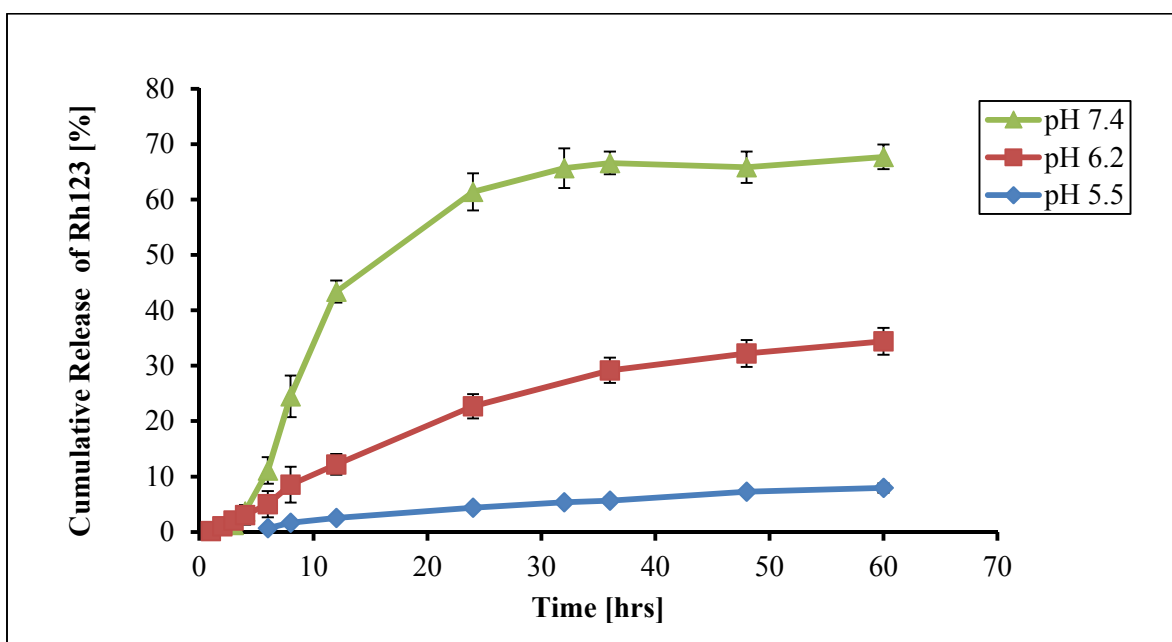


Figure 10: pH-dependent release of Rh123 from Eudragit L-100 NPs. Rh123-containing NPs were incubated at room temperature in PBS pH 5.5, 6.2 and 7.4. Samples were removed at different time points and Rh123 concentration was quantified spectrofluorometrically (EX = 485 nm, EM = 520 nm). Results are shown as mean \pm SD. (n = 3).

The cumulative Rh123 profiles shown in Figure 10 underline a pH-dependent release process that can be attributed to the hydrolysis in the ester backbone of the Eudragit L-100 co-polymer. The total cumulative dye release from the NPs at pH 7.4 was 67.7 ± 2.2 %. Under more acidic conditions, the amount of Rh123 that appeared in solution was dramatically reduced (37.5 ± 0.8

% at pH 6.2 and 11.5 ± 1.0 % at pH 5.5 respectively). This suggests that Rh123 release from Eudragit L-100 NPs under reduced acidic conditions present in TB-infected phagosomes will be 3-fold greater than in non-infected macrophages where lysosomal pH remains between pH 4.7-5.5. The lag time of Rh123 release observed at pH 7.4 increases the confidence that only a small fraction of Eudragit L-100-encapsulated payload will be prematurely released in the alveolar region prior to internalization of NPs by AMs.

To delineate underlying mechanisms that govern release of Rh123 from Eudragit L-100 NPs, release profiles were analyzed using various mathematical models. The results from model-dependent linear and non-linear regression analyses are summarized in Table 4.

Table 4. Mathematical Assessment of Rh123 Release Kinetics

pH 5.5						
	Zero	First	Higuchi	Hixon	Baker	Peppas
R ²	0.947	0.974	0.992	0.927	0.983	0.976
pH 6.2						
	Zero	First	Higuchi	Hixon	Baker	Peppas
R ²	0.921	0.997	0.978	0.975	0.993	0.963
pH 7.4						
	Zero	First	Higuchi	Hixon	Baker	Peppas
R ²	0.890	0.997	0.868	0.953	0.993	0.821

From the correlation coefficients summarized in Table 4, it appears that not only one but several different release mechanisms may have contributed to the experimentally determined appearance rates of Rh123. To verify the goodness of fit for the various release models, an analysis of residuals was performed for each condition and residual plots for each of the mathematical models were generated (see Appendix). Limited by the numbers of experimental observations, it was concluded that more than one model can adequately explained the release kinetics of Rh123 from this NP dispersion. According to the pattern of residuals, however, it appeared that Rh123 release at pH 5.5 closely followed the Higuchi model. At pH 6.2, first order kinetics adequately described Rh123 release, whereas Rh123 release at pH 7.4 appeared to follow first order kinetics and as well as the Baker model.

4.2. Alveolar Macrophages Cell Culture Model

Eudragit L-100 NPs are predicted to effectively accumulate in AMs in order to maximize therapeutic drug concentration against macrophages-resident TB bacteria. The mouse alveolar macrophage MH-S cell line was selected for *in vitro* uptake studies using the fabricated NPs. The initial objective was to define an experimental design that assures sufficient cells for cellular uptake experiments despite repeated washing. To accomplish this objective, pilot experiments were conducted to identify suitable seeding densities and cell attachment periods. Total protein concentration after cell lysis was used as a quantitative estimate of cells remaining. The correlation between total cellular protein and cell number was assessed using linear regression analysis of cells versus protein amount after lysis:

$$\text{Total cell protein} = 0.0003 \times \text{Cell number} - 1.1238$$

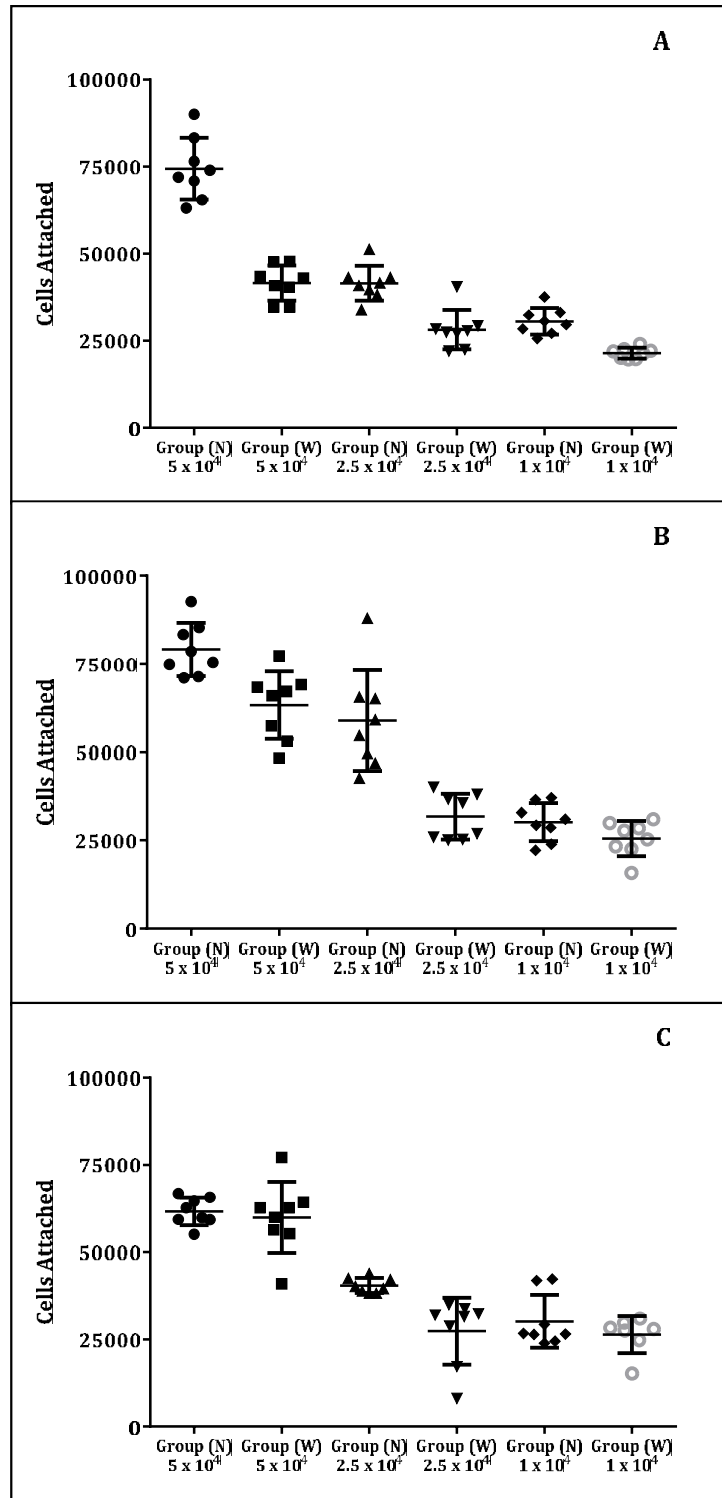


Figure 11: Optimization of MH-S cell attachment. MH-S cells were seeded at different densities in 96-well plate and incubated at 37° C (5% CO₂). The cell number remaining after 12 hours (Panel A), 24 hours (Panel B), and 48 hours (Panel C) with (W) and without (N) washing was estimated using the BCA protein assay. Results are shown as mean ± SD (n = 8).

The results summarized in Figure 11 suggest that a cell seeding density of 5×10^4 cells/well incubated for 48 hours is most resistant to washing manipulations when compared to control experiments without washing ($p = 0.65$). Therefore, all subsequent cell culture experiments were performed using a seeding density of 5×10^4 cells/well, and experiments were only initiated after incubation period of 48 hours.

4.2.1. Cell Viability Studies

To assess the consequences of Eudragit L-100 NP exposure on cell viability, increasing concentrations of the NP suspension were incubated with MH-S cell line for up to 6 hours before cell viability was estimated using the CellTiter-Glo® Luminescent Cell Viability Assay. The results summarized in Figure 12 demonstrated that increasing NP concentrations progressively decreased MH-S cells viability even after a short-term incubation period of only 1 hour.

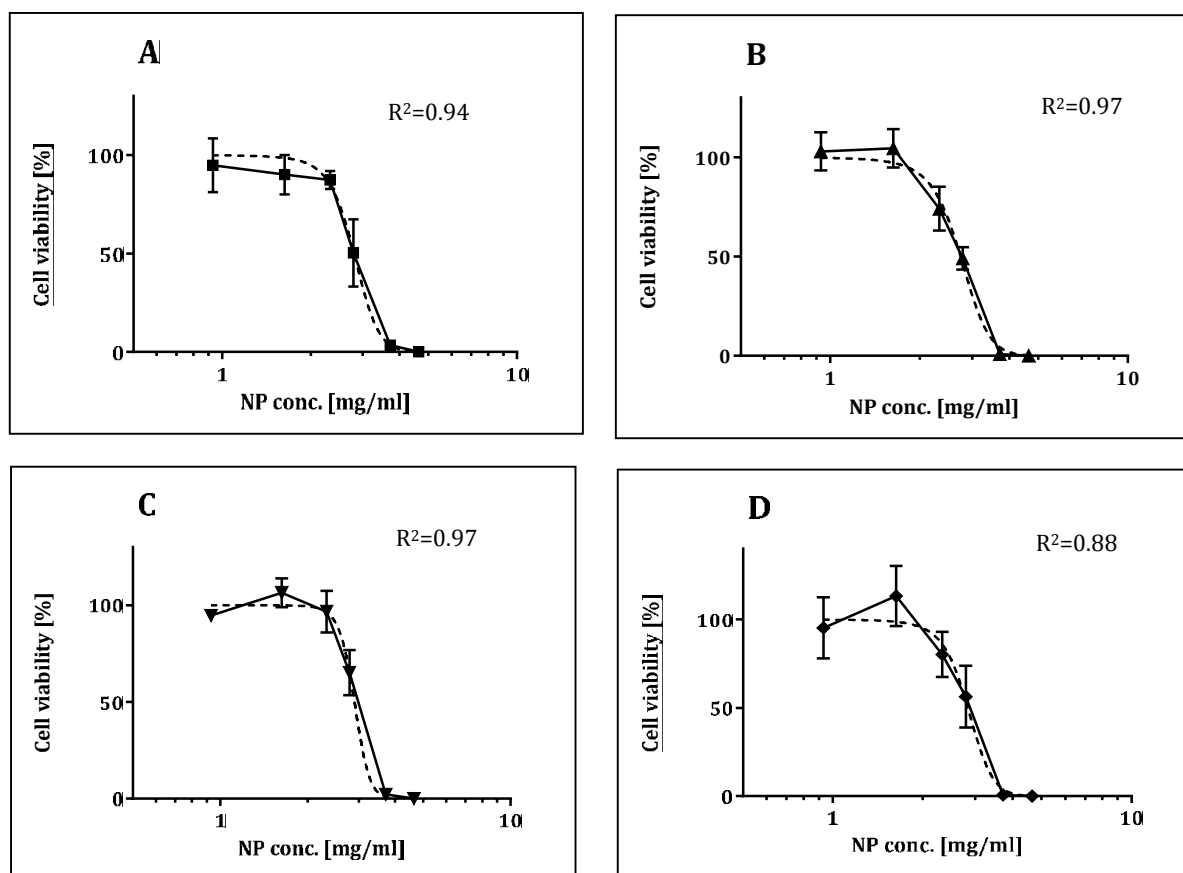


Figure 12: Cytotoxicity of Eudragit L-100 nanoparticles on MH-S cells *in vitro*. MH-S cells were incubated at 37° C (5% CO₂) in 96-well plates for 1 hour (Panel A), 2 hours (Panel B), 4 hours (Panel C), and 6 hours (Panel D) with NP suspension ranging from 0.93 to 4.65 mg Eudragit L-100/mL. Viability data are normalized to vehicle-treated control. Dotted line represents fitted line of non-linear regression analysis (see Materials and Methods). Results are shown as mean ± SD (n = 3).

To compare time-dependent effects of NP on MH-S cell viability, the concentration inducing 50% cytotoxicity (IC₅₀) was estimated using non-linear regression analysis (see Materials and Methods). The IC₅₀ values for different incubation times are summarized in Table 5. In the absence of significant differences between those values, it is concluded that decreased cell viability is most likely induced by an acute toxicity mechanism in response to Eudragit L-100 NP exposure.

Table 5. Effect of Eudragit L-100 Nanoparticles on MH-S Cell Viability *in vitro*

Incubation time [hrs]	IC50 [mg/mL]
1	2.82 ± 0.15
2	2.73 ± 0.16
4	2.91 ± 0.14
6	2.83 ± 0.35

Results are shown as mean ± SD (n = 3).

Based on these data, subsequent cellular uptake studies were performed using a NP concentration of 1.62 mg/mL, which is estimated to compromise cell viability <0.1%.

4.2.2. Nanoparticles Uptake by Alveolar Macrophages

To quantify intracellular accumulation of Eudragit L-100 NPs in MH-S cells, cellular uptake of Rh123-loaded NPs was compared to the uptake of a Rh123 solution prepared in DMEM at a concentration equivalent to the Rh123 concentration administered as NP suspension. The fluorescence signal of intracellular Rh123 was measured spectrofluorometrically before and after cells lysis.

The results summarized in Figure 13 suggest that MH-S cells are capable of internalizing Rh123-containing NPs to the same extent as Rh123 dissolved in serum-free cell culture media.

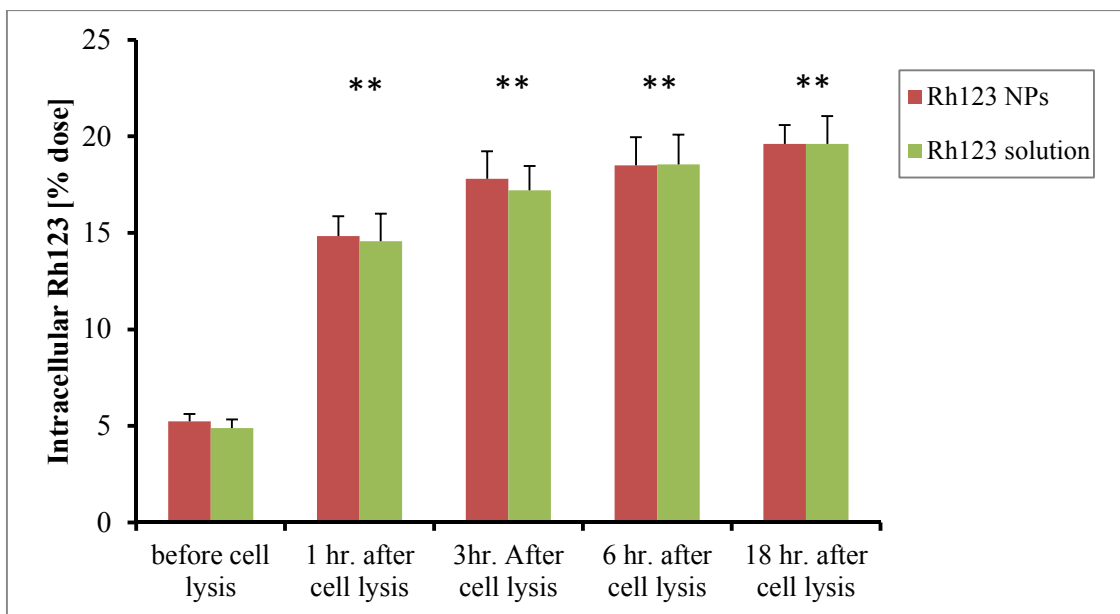


Figure 13: Uptake of Rh123-containing Eudragit L-100 NPs in MH-S cells. NP suspension and Rh123 solution prepared in serum-free DMEM were incubated with MH-S cells for 30 minutes. Fluorescence was quantified at EM = 520 nm (EX = 485 nm) before and after lysis of cells using RIPA buffer. Fluorescence signal after cell lysis was monitored for up to 18 hours. Results are shown as mean \pm SD. (n = 6). ** significantly different $p < 0.001$

It is concluded that cellular uptake of NPs and Rh123 solution in MH-S cells may not require specific membrane interactions but rather occurs via non-specific engulfment of extracellular fluid. The experiment demonstrated that the captured fluorescence signal of Rh123 significantly increased after dissolving the cells with RIPA lysis buffer. This suggests fluorescence quenching of Rh123 after cellular uptake due to high concentrations of internalized material within small intracellular compartments (e.g., lysosomes). Consequently, accurate determination of internalized Rh123 requires destruction of cellular and subcellular compartments allowing homogeneous distribution of this fluorescence probe. Time-dependent monitoring of the fluorescence signal demonstrated that RIPA buffer instantaneously dissolves

all cellular and subcellular membrane structures facilitating accurate quantification of Rh123 after cell lysis within one hour.

4.2.3. Modulation of Lysosomal pH Values

One major objective of this research was to assess the impact of acidic lysosomal pH in TB-infected AMs on NPs uptake and Rh123 release kinetics. Previously, it was recognized that fluorescence intensity of FD40 quantitatively changes in response to different pH values. Consequently, this fluorescent probe has been widely used to estimate the pH value of intracellular compartments, including lysosomes (Ohkuma et al., 1978). To quantify lysosomal pH in MH-S cells, a pH-dependent calibration curve of FD40 fluorescence was generated (see Figure 14).

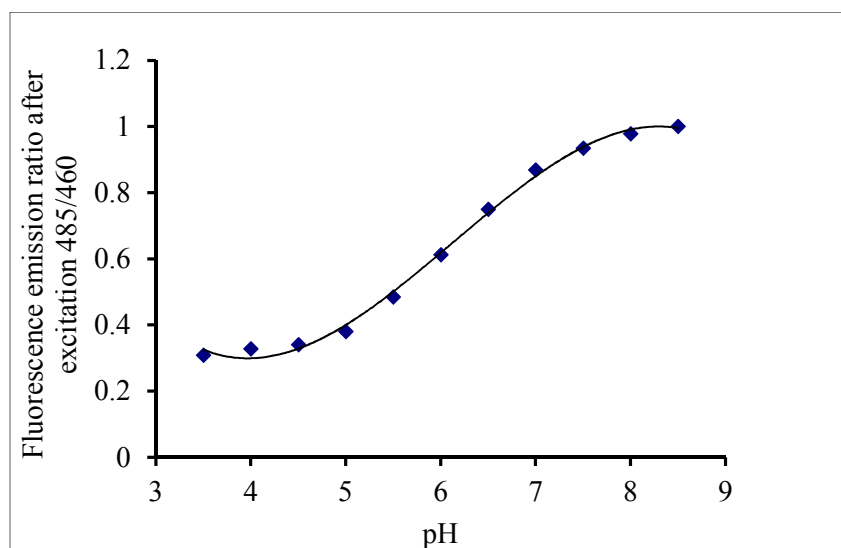


Figure 14: pH-dependent fluorescence of FD40. The fluorescence of FD40 dissolved at 1 $\mu\text{g/mL}$ in phosphate buffer pH 3.5-8.5 was measured at EM = 520 nm using EX = 485 nm and EX = 460 nm, respectively.

From the fluorescence ratio measured at EM = 520 nm using two different EX wavelengths, it is evident that the fluorescence of FD40 measured at EX = 485 nm is changing more rapidly under basic conditions than the intensity acquired at EX = 460 nm. Using polynomial least square regression analysis, the experimental relationship shown in Figure 14 can be mathematically described by:

$$\text{Fluorescence FD40 (485/460)} = -0.0173 \text{ pH}^3 + 0.3183 \text{ pH}^2 - 1.7085 \text{ pH} + 3.1481$$

This equation was used to estimate lysosomal pH after measuring the EM intensity ratio at EX = 485 and 460 nm, respectively.

Prior to lysosomal pH measurement, it was crucial to define experimental conditions that allow maximum accumulation of FD40 inside the desired subcellular compartments, which will increase quantitative accuracy of lysosomal pH estimates. Figure 15 summarize the effect of different extracellular FD40 concentrations and incubation periods on intracellular FD40 accumulation in MH-S cells.

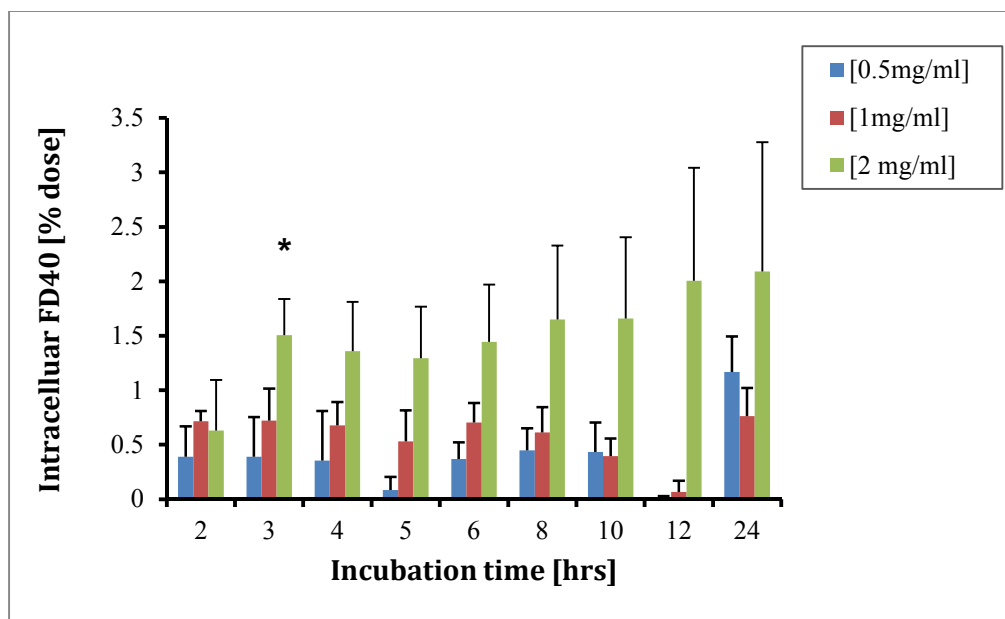


Figure 15: FD40 uptake kinetics in MH-S cells. FD40 solutions prepared in serum-free DMEM were incubated with MH-S cells at 37° C for up to 24 hours. After quenching of extracellular FD40 using Trypan blue, fluorescence was quantified spectrofluorometrically at EM = 520 nm (EX = 485 nm). Results are shown as mean ± SD (n = 5).

* significantly different $p < 0.05$

The results in Figure 15 demonstrate a dose-dependent uptake of FD40 in MH-S cells, with a maximum intracellular accumulation of this pH-sensitive macromolecule after a 3-hour incubation period using 2 mg/mL of FD40. Prolonged incubation did not significantly increase intracellular FD40 levels. Consequently, preincubation of MH-S cells with a 2 mg/mL FD40 solution for 3 hours was adopted as a standard experimental design for measuring lysosomal pH in MH-S cells.

Since extracellular FD40 was not removed by washing in order to minimize the risk of cell loss, Trypan blue was used to quench residual extracellular probe prior to spectrofluorometric quantitation of intracellular FD40 (Nuutila et al., 2005). To evaluate the effectiveness of Trypan blue in FD40 quenching, different dye concentrations (0.2 - 4 mg/mL) were combined with a

FD40 solution that was prepared at 1 mg/mL using phenol red-containing, serum-free DMEM, phenol red-free, serum-free DMEM, and PBS.

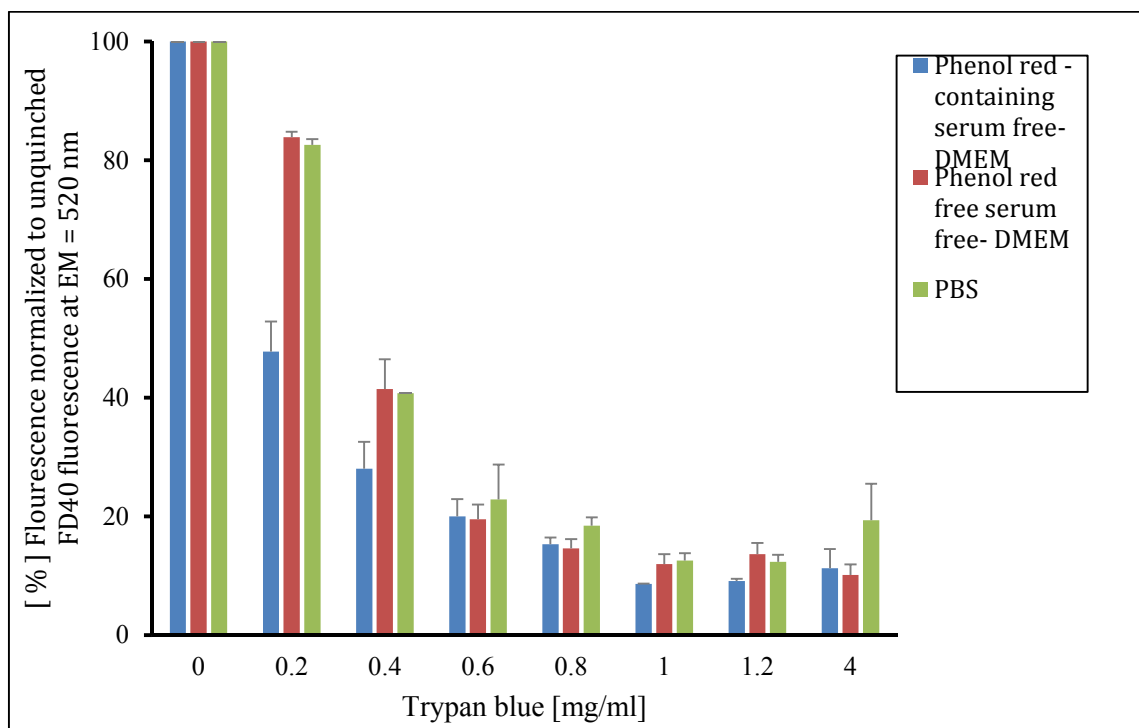


Figure 16: Quenching efficiency of FD40 using Trypan blue. Fluorescence intensity of FD40 (1 mg/mL) was measured at EM = 520 nm (EX = 485 nm) and normalized to unquenched control. Results are shown as mean \pm SD (n = 2).

The data summarized in Figure 16 demonstrated a constant decrease in FD40-associated fluorescence signal when combined with increasing Trypan blue concentrations. However, even at the highest Trypan blue concentration of 4 mg/mL, which was reported to be safe for use in cell culture experiments, a residual FD40 fluorescence signal was detected. Since accurate measurement of lysosomal pH critically depends on quenching of extracellular FD40, it was concluded that addition of Trypan blue was not a viable approach to accomplish the objective of this study. Instead, additional washing steps must be included to eliminate excess extracellular FD40 despite the increased risk of removing attached cells during this manipulation.

After modification of the experimental procedure required to remove extracellular FD40, it was necessary to repeat cellular FD40 uptake studies. In comparison to the 2-hour incubation period, intracellular FD40 amount was significantly increased after a 3-hour incubation (Figure 17, Panel A). More extended incubation did not augment uptake efficacy.

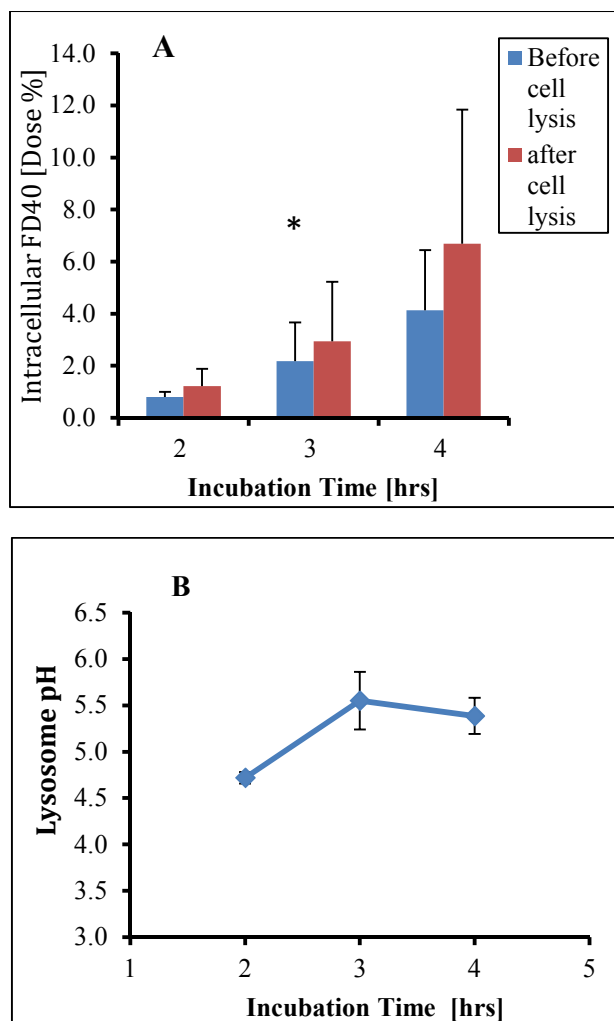


Figure 17: Estimation of lysosomal pH in MH-S cells. Panel A: FD40 (2.5 mg/mL) in serum-free DMEM was incubated with MH-S cells for up to 4 hours. After removal of extracellular FD40 by washing, intracellular FD40 was quantified before and after cell lysis spectrofluorometrically at EM = 520 (EX = 485 nm). Panel B: Estimated lysosomal pH value of MH-S cells using FD40 pH-dependent calibration curve. Results are shown as mean \pm SD. (n = 7).

* significantly different $p < 0.05$

Using the pH-dependent calibration curve of FD40, the lysosomal pH of control MH-S cells was estimated to be in the range of pH 4.7 – 5.6 (Figure 17, Panel B), which is consistent with previously reported values (Geisow et al., 1981).

To quantitatively assess cellular uptake and intracellular release of Rh123-containing NPs under pH conditions present in the phagosomes of TB-infected macrophages, experimental modulation of lysosomal pH was attempted using procedures previously established by several research groups (Ohkuma et al., 1978, Poole et al., 1981, and Geisow et al., 1981).

MH-S cells were treated with different concentrations of NH_4Cl which is predicted to elevate the pH of lysosomes from pH 5.5 to the desired value of approximately pH 6.2 (Hackam et al., 1997).

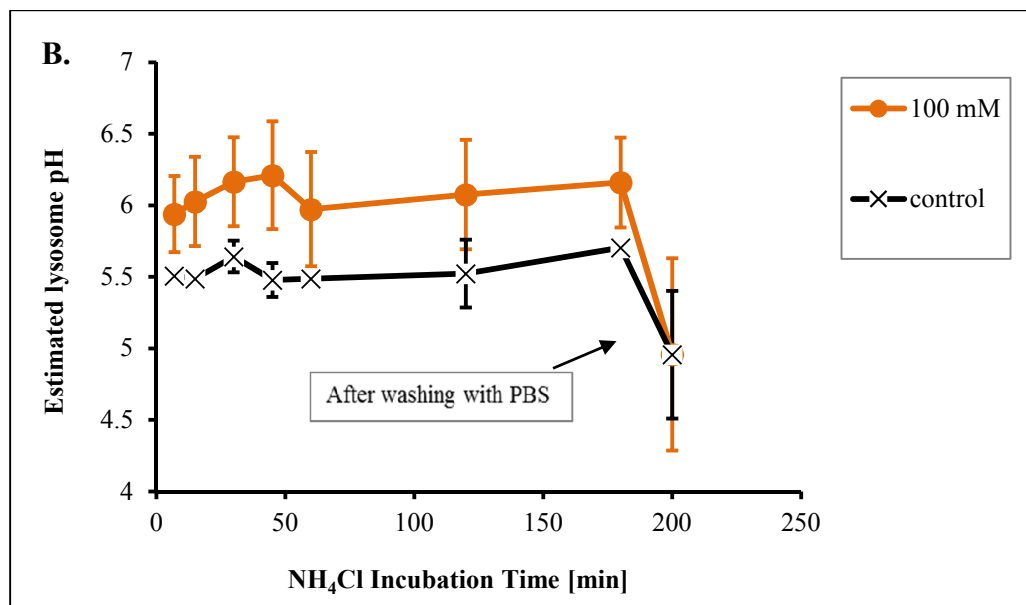
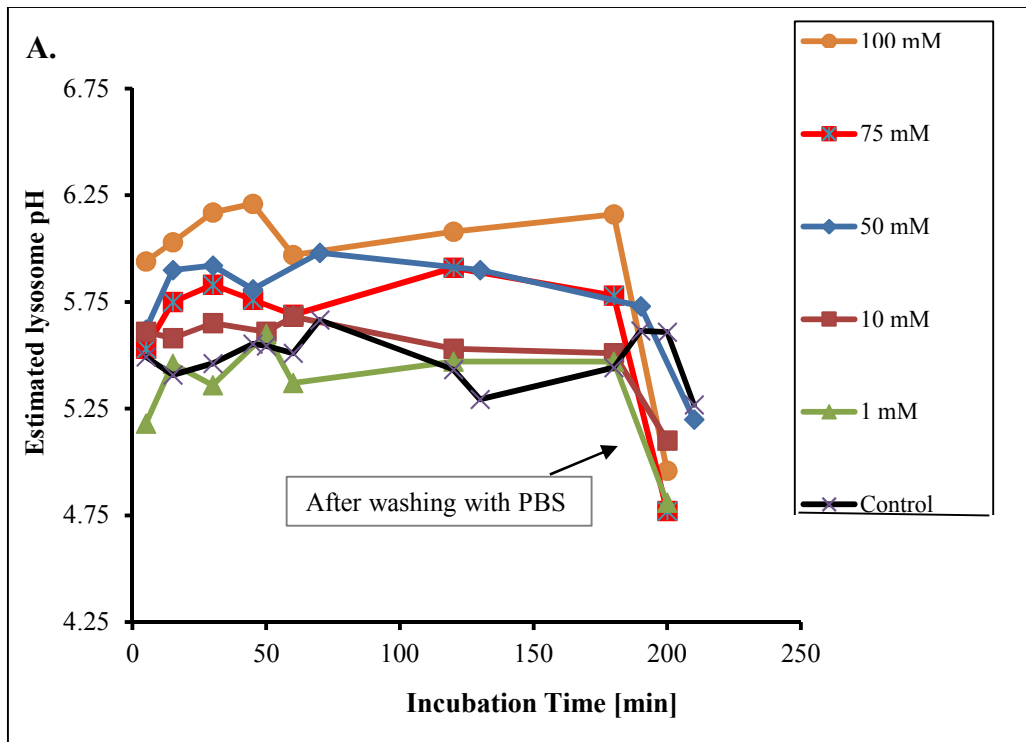


Figure 18: Lysosomal pH modulation in MH-S cells. NH₄Cl solutions prepared in amino acid-free DMEM were incubated with MH-S cells for 1 hour in 37° C. Lysosomal pH was estimated using pH-dependent fluorescence of intracellular FD40. Amino acid-free DMEM was used as control (see Materials and Methods). Panel A: mean estimated pH values of lysosomes after NH₄Cl treatment (n = 6). Panel B: effect of 100 mM NH₄Cl on lysosomal pH of MH-S cells. Results are shown as mean ± SD. (n = 6).

The results summarized in Figure 18 Panel A illustrate that NH_4Cl concentrations >10 mM effectively increased lysosomal pH of MH-S above the resting pH value of 5.5. Incubation with 100 mM NH_4Cl solution raised lysosomal pH to the desired value of 6.2 within 50 minutes. Closer examination of the changes induced by 100 mM NH_4Cl solution revealed that significantly less acidic lysosomal pH values are achieved within 5 minutes (Panel B). Removal of external NH_4Cl by washing resulted in rapid re-acidification of lysosomes, which is likely due to compensatory mechanism induced by the action of acidifying enzymes such as the V-ATPase.

4.2.4. Lysosomal pH Effect on Nanoparticles Uptake in MH-S Cells

After establishing a suitable experimental procedure to modulate lysosomal pH to the less acidic value present in TB-infected macrophages, it was necessary to investigate whether changes in lysosomal pH affect cellular uptake efficiency of MH-S cells. The results summarized in Figure 19 underline a significant decrease in intracellular accumulation of both Rh123-containing NPs as well as Rh123 administered as a solution after cells were treated with 100 mM NH_4Cl . Cellular lysis still increased the fluorescence intensity of internalized Rh123 supporting the earlier hypothesis of quenching due to accumulation in subcellular compartments.

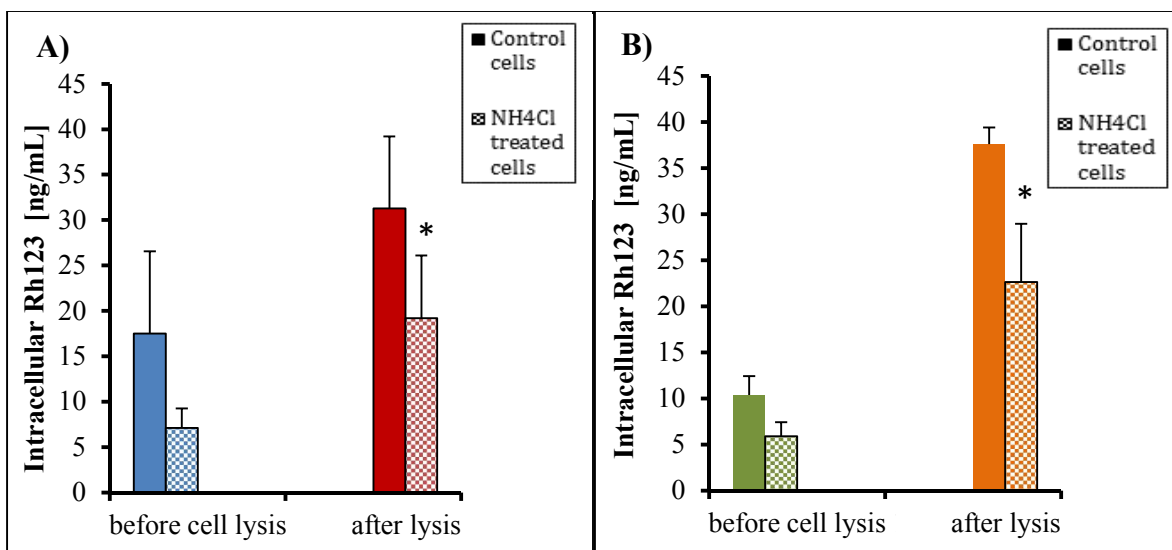


Figure 19: Effect of lysosomal pH on internalization efficiency. Rh123–loaded NPs (Panel A) and a Rh123 solution prepared a a concentration equivalent to NP-encapsulated Rh123 (Panel B) were incubated with MH-S in the presence and absence of 100 mM NH₄Cl for 1 hour at 37° C. Intracellular Rh123 was quantified before and after cells lysis spectrofluorometrically at EM = 520 nm (EX = 485 nm). Control cells were subjected to amino acid–free DMEM. Results are displayed as mean ± SD. (n = 4).

* significantly different p <0.05

Whether this reduced cellular uptake capacity after NH₄Cl treatment was uniquely associated with the use of this chemical or due to the induced increase lysosomal pH requires further investigation. Similar to earlier observations, NP uptake as well as Rh123 uptake after administration as a solution was reduced equivalently suggesting the possibility of the same cellular uptake mechanism.

MH-S cells incubated with Rh123-containing Eudragit L-100 NPs and the Rh123 solution were visually evaluated by confocal microscope in order to investigate whether distinct intracellular distribution pattern can be observed. This qualitative methodology could be used to monitor different release kinetic of Rh123-containing NPs inside MH-S cells in response to different lysosomal pH values. Representative confocal images are shown in Figure 20 where the

presence of the light green color visually underlines successful internalization of Rh123-containing NPs and Rh123 administered as a solution in MH-S cells (Panel A and C). Modulation of lysosomal pH using 100 mM NH_4Cl quantitatively reduced cellular uptake of extracellular NPs and Rh123 (see Figure 19). However, the difference in quantitative uptake using NH_4Cl -treated cells is not effectively visible in confocal images (Panel B and D).

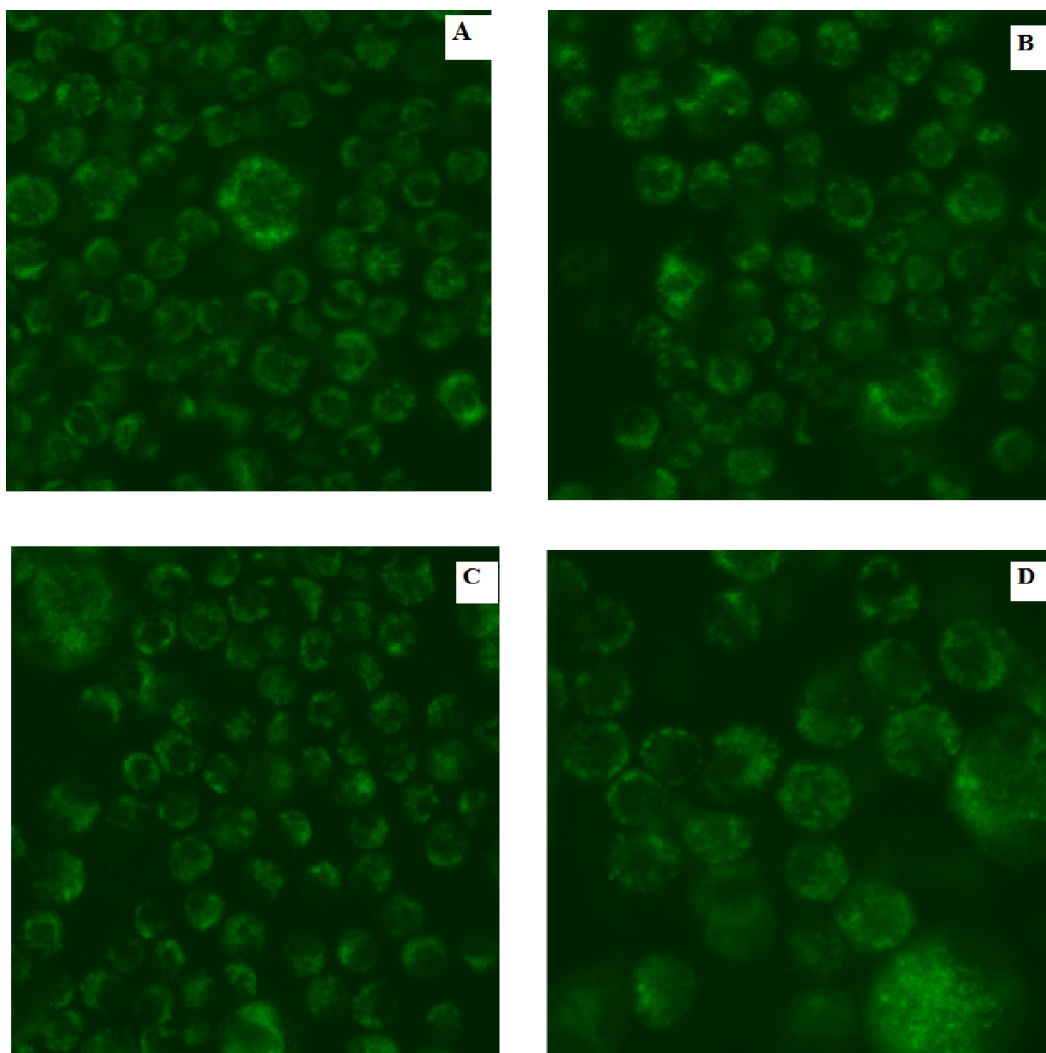


Figure 20: Visualization of cellular uptake of Rh123-containing Eudragit L-100 NPs. MH-S cells were incubated for 1 hour at 37° C with Rh123-containing Eudragit L-100 NPs or Rh123 solution prepared in amino acid-free DMEM in the presence and absence of 100 mM NH_4Cl . Representation confocal images were acquired at EM = 505-530 nm (EX = 488 nm) using the Zeiss LSM 510 META. Panel A: Rh123-NPs in control cells, Panel B: Rh123-NPs in NH_4Cl -treated cells, Panel C: Rh123 solution in control cells, and Panel D: Rh123 solution in NH_4Cl -treated cells.

It was hypothesized that Rh123 release from intracellular Eudragit L-100 NPs can be visualized by a change in subcellular distribution pattern of the highly fluorescent NP that accumulated in lysosomes after cellular internalization. However, comparison of the fluorescence pattern acquired by confocal microscopy for Rh123-containing Eudragit L-100 NPs and Rh123 solution (Figure 20, Panel A and C) did not support this hypothesis. These unexpected findings revealed a limitation of confocal microscope to determine intracellular release kinetics of Rh123-containing Eudragit L-100 NP in response to different lysosomal pH conditions.

5. Discussion

The emergence of drug-resistant TB strains decreases the effectiveness of conventional drug regimens, augments the risk of transmission, and imposes critical conditions for immunocompromised individuals. Development of novel drug delivery systems that allow spatial and temporal control of drug release in response to unique, disease-associated changes in lysosomal pH of TB-infected AMs offer the advantage for selective intervention at the target site. Simultaneously, drug exposure of healthy tissues will be limited, which is anticipated to decrease adverse events. The less acidic environment present in the phagosome of *M. tuberculosis*-infected AMs (i.e., pH = 6.2 instead of pH = 4.7-5.5) was used as scientific rationale for exploring nanoparticle formulations fabricated using the pH-responsive polymer Eudragit L-100. The main hypothesis driving this research was that NP payload is preferentially released inside the phagosome of infected AMs where the less acidic environment favors accelerated degradation of the acrylic acid/methylacrylate co-polymer. Although uninfected AMs may internalize these NPs at the same rate, it was predicted that payload release will be significantly slower due to the more acidic environment. Consequently, drug exposure of uninfected AMs will be limited resulting in greater safety for patients.

The fluorescent dye Rh123 was selected as surrogate payload to facilitate rapid fluorometric quantitation of the encapsulation efficiency in Eudragit L-100 NPs, *in vitro* release under different pH conditions, and intracellular accumulation in MH-S cells. Rh123 exhibits physicochemical characteristics comparable to the anti-TB drug rifampicin, specifically with regards to molecular lipophilicity as demonstrated by similar solubility in organic solvents such as methanol, ethanol, and dimethyl sulfoxide (Santa Cruz Biotechnology, 2015).

Rh123 containing–Eudragit L100 NPs were fabricated using the nanoprecipitation method. Conventionally, the polymer is dissolved in a suitable organic solvents including acetone (Devarajan et al., 2007), methanol (Karve et al., 2011), and ethanol (Tang et al., 2011). To enable sufficient solubility of Eudragit L-100 and the fluorescent dye, an acetone/water mixture (97:3, v/v) was selected for this research. Acetone was also preferred because of its high evaporation rate at room temperature (vapor pressure at 25 °C = 229 mm Hg (DDBST, 2015)), which was predicted to limit residual solvent in the NP preparation that may induce a cytotoxic effect in MH-S cells.

To maximize exposure of TB-infected AMs to this novel stimulus-induced drug delivery system, fabricated NPs were intended for administration via inhalation. Consequently, it was essential to optimize fabrication conditions with a specific focus on particle size as this parameter predominantly defines pulmonary deposition after inhalation (Labiris et al., 2003). Previous research focusing on pulmonary administration of insulin-loaded liposomes in mice identified a critical particle diameter of approximately 250 nm for successful deposition in the alveolar region (Huang et al., 2006). Larger particles accumulated at extrathoracic sites such as the larynx, whereas particles ≤ 50 nm were reported to induce autophagy of macrophages (Eidi et al., 2011). The efforts of extensive optimization experiments identified a polymer feed of 100 mg of Eudragit L-100 combined with a 3-hour magnetic stirring period that result in in NPs exhibiting a desired diameter of approximately 250 nm. At the end of the fabrication process, Rh123-containing NPs were subjected to an additional purification step by dialysis in 0.3 μ M HCl (pH = 3.5) to remove surface-adsorbed Rh123 that was predicted to induce an undesired burst effect after administration. The acidic dialysis medium was selected with the objective to

limit Eudragit L-100 degradation as well as premature release of the encapsulated payload during purification.

Accurate analytical determination of encapsulated Rh123 in Eudragit L-100 NPs requires complete dissolution of the polymer matrix and subsequent release of the fluorescent dye into the dissolution vehicle. Initially, several organic solvents were evaluated based on available solubility data for Eudragit L-100. Surprisingly, particle suspensions prepared in these solvents contained a significant fraction of larger aggregates $\geq 1 \mu\text{m}$. Billmeyer and colleagues hypothesized that the process of polymer dissolution is a sequential process involving polymer swelling followed by dissolution of the solvent-accessible polymer strands (Billmeyer Jr., 1984). Eudragit L-100 is a copolymer comprised of methacrylic acid and methyl methacrylate at a molar ratio of 1:1. Consequently, it was predicted that inter- and intramolecular forces such as hydrogen bonding and dipole-dipole interactions govern solvation. As shown in Figure 7, NP dispersion prepared in acetone, isopropanol, and ethanol contained large aggregates $>1 \mu\text{m}$. These results suggested that cohesive polymer-polymer forces between Eudragit L-100 NPs were greater than adhesive polymer-solvent forces. Upon addition of NaOH, the fraction of large aggregates disappeared most likely due to ionic forces between hydroxyl groups and carboxylate groups of deprotonated methacrylic acid. Ultimately, base-catalyzed ester bond hydrolysis of the methylmethacrylate backbone may have led to the complete dissolution of the Eudragit L-100 NPs (Taylor, 2002).

The release properties of Rh123 from fabricated Eudragit L-100 NPs were assessed using phosphate buffer solution adjusted to pH values that were representative of the highest pH value recorded inside lysosomes of uninfected control macrophages (pH 5.5) (Butor et al., 1995), the lowest pH value measured in *M. tuberculosis*-containing phagosomes (pH 6.2) (Sturgill-

Koszycki et al., 1994), and the pH value estimated within the bronchial lumen (pH 7.4). Various mathematical models were used to delineate the mechanisms governing Rh123 release from Eudragit L-100 NPs under different pH conditions. The highest correlation coefficients from regression analyses and residual profiles obtained for first-order release kinetics suggested polymer backbone erosion induced by partial ionization of Eudragit L-100 carboxylate groups as a dominant mechanism of payload release at pH 6.2 and 7.4. Model-dependent analysis of release kinetics at pH 5.5 revealed the highest correlation for the Higuchi model indicating that Rh123 diffusion through the intact NP is dominating payload release under more acidic conditions where carrier erosion is minimal. The analysis of residuals illustrated that not only one but multiple mathematical models may explain the release kinetics of Rh123 from Eudragit L-100 NPs at pH values tested. More extended studies will be required to collect a greater number of data points that will increase confidence in model-dependent correlation analyses.

Cellular uptake experiments using Rh123-containing NPs and Rh123 solution revealed that MH-S cells contained the same amount of Rh123 irrespective to the delivery system applied. There are several mechanisms known to facilitate intracellular uptake. However, phagocytosis is predicted to dominate internalization of particulate material in macrophages (Sahay et al., 2010). This uptake mechanism is triggered by an interaction of foreign material with cell surface receptors such as mannose and scavenger receptors. Other receptors participating in this recognition include the complement receptor and Fc receptors, which can bind to complement molecules or immunoglobulins adsorbed to the particle surface (Sahay et al., 2010). Factors such as NP material, size, and shape, as well as cell type determine the magnitude of NP uptake by phagocytosis (Kuhn et al., 2014). Whether or not receptors were involved in MH-S uptake of Eudragit L-100 NPs is unclear. Future experiments using various pharmacological inhibitors of

cellular internalization mechanisms may allow further delineation of the underlying mechanism of NP uptake in this model system of TB-infected AMs (Ivanov, 2008).

In contrast, cellular uptake of solutes dissolved in extracellular fluid is primarily accomplished via pinocytosis, which involves engulfment of an extracellular volume within a small membrane vesicle. This uptake mechanism is actin-driven and involves protrusions of the outer cell membrane followed by fusion with the cell membrane (Doherty et al., 2009). It was predicted that uptake of Rh123 solution will be predominantly accomplished by pinocytosis. Comparable extent of intracellular Rh123, however, requires further assessment of this hypothesis.

The discovery that intracellular Rh123 concentrations increase after dissolving cellular and subcellular compartment using RPA lysis buffer suggested quenching of internalized fluorescent dye due to confined accumulation inside a small cellular compartment such as the lysosome. Solubilization of these compartments allows homogeneous distribution of Rh123 within the cell lysate and, thus, accurate quantitation using fluorescence spectrophotometry.

FITC-labelled Dextran (FD40; M.W. = 40,000) is a commercially available fluorescent compound that has been widely used for the assessment of lysosomes pH due to preferential sequestration these organelles (Geisow et al., 1981). The measured fluorescence intensity of this probe using emission filters of 520 nm is very sensitive to the pH, especially in the range of 5 to 7.5. Ohkuma and colleagues showed that the FD fluorescence spectrum displays a sharp peak in alkaline medium upon excitation with 495 nm. Under more acidic conditions, this peak intensity decreases and is replaced by another peak at 450 nm (Ohkuma et al., 1978). Consequently, FD40 fluorescence was measured in PBS at different pH values using emission filter 520 nm with excitation filters of 485 nm (bandwidth = 10 nm) and 460 nm (bandwidth = 10 nm). These

excitation filters possess the same fluorescence detection sensitivity as determined by Fluorescence SpectraViewer (Life Technologies, Grand Island, NY). Subsequently, the yield ratio 485/460 was calculated, and calibration curve was used to predict the pH of MH-S alveolar macrophages lysosomes.

To simulate lysosomal pH conditions of *M. tuberculosis*-infected macrophages, MH-S macrophages were subjected to different concentrations of NH_4Cl that has been used previously to increase lysosomal pH value in different cell lines (Ohkuma et al., 1978, Poole et al., 1981, and Geisow et al., 1981). NH_4Cl was dissolved in amino acid free- and fetal bovine serum-free DMEM to limit undesired ammonia production due to cellular metabolism of these compounds (Ohkuma et al., 1978). Experimental data summarized in Figure 18 confirm a concentration-dependent increase in lysosomal pH. This effect was reversed when the NH_4Cl solution was removed by washing. The mechanism by which NH_4Cl affects lysosomal pH is attributed to the free base (i.e. NH_3) (De Duve et al., 1974). Upon incubation with macrophages, ammonia diffuses across the cell membrane entering the lysosomal compartment. The acidic environment inside the lysosomes, which is maintained by acidifying enzymes, will facilitate NH_3 ionization to NH_4^+ that will be trapped inside the lysosomes as an ionized species. The ammonia concentration available for neutralization of the acidic environment in lysosomes is defined by the extracellular NH_4Cl concentration used. Upon removal of extracellular NH_4Cl solution, NH_4^+ will slowly leak out of the lysosomes, and enzymes/carriers like Na^+/K^+ -ATPase and V-ATPase will continue to acidify the lumen until lysosomal pH conditions are re-established.

Based on the predicted, distinctly different cellular uptake mechanisms for NPs and solutions, it was hypothesized that confocal microscope may be a suitable qualitative technique to visually distinguish intracellular Rh123 after release from NPs. As the results from comparative uptake

experiments using Rh123-containing NPs and Rh123 solution did not reveal a significantly different intracellular distribution pattern (see Figure 20), alternative approaches as discussed in the Future Directions section must be considered.

6. Conclusions

Therapeutic efficacy of anti-TB drugs is limited due to the requirement for prolonged drug administration and debilitating drug-induced adverse effects that promote patients non-compliance with drug regimens, and consequently, treatment failure. Nanotechnology-based SMART drug delivery systems may offer unique advantages in reducing incidence of drug-resistant TB while limiting undesirable adverse events that are usually associated with non-selective drug distribution after systemic administration of conventional anti-TB drugs.

In this research, the nanoprecipitation method was successively applied to fabricate Rh123-containing Eudragit L-100 NPs of approximately 250 nm in diameter, which are suitable to reach AMs after pulmonary administration. Eudragit L-100 concentrations ≤ 1.62 mg/mL did not induce significant cytotoxicity in MH-S cells. Furthermore, experimental conditions were established to mimic less acidic lysosomal environment present in TB-infected macrophages using 100 mM NH_4Cl solution.

Rh123 release from Eudragit L-100 NPs was pH-dependent with a 3-fold greater release at pH 6.2 than at pH 5.5. These data suggest significantly faster release of NP-encapsulated payload in TB-infected AMs that harbor *M. Tuberculosis* inside their phagosomes. In the absence of significant burst release at pH 7.4, it is predicted that NPs will be internalized by AMs after pulmonary administration without premature release of the encapsulated payload in the lumen of alveoli.

7. Future Directions

It was anticipated that confocal microscopy will be a suitable technology to qualitatively differentiate between NP-associated and released Rh123 according to a significantly different intracellular fluorescence distribution pattern. Unfortunately, the results from this study did not support this hypothesis leaving a major question of this research unanswered. Future effort should be directed toward suitable methodologies that facilitate qualitative and quantitative measurement of intracellular distribution of NP-encapsulated payload.

It is proposed that cell fractionation, which physically separate subcellular compartments (de Duve et al., 1953), may offer the best chances for success. In general, this technique is comprised of two separate centrifugation steps: (1) differential centrifugation, which relies on the difference in terminal velocity of cellular components, will separate cellular components on the basis of size, mass and density into several zones (de Duve et al., 1953). Differential centrifugation is not organelle-specific because each zone contains several types of organelles having similar sedimentation velocities. Therefore, density gradient centrifugation will be required to separate lysosomes from other organelles. Purified lysosomes can then be incubated with Rh123-NPs and release kinetics of Rh123 from Eudragit L-100 NP can be quantified spectrofluorometrically as Rh123 diffuses out of the lysosomes into the suspension vehicle.

To circumvent this tedious centrifugation methodology, Eudragit L-100 NPs containing rifampicin could be prepared. Release kinetics and therapeutic efficacy can be evaluated *in vitro* by incubating rifampicin-NPs with TB-infected AMs collected from TB-infected animals. Alternatively, rifampicin-containing Eudragit L-100 NPs can be administered via inhalation to animals, and AMs uptake as well as therapeutic efficacy can be assessed by sacrificing animals at predetermined time intervals. In both cases, macrophages will be collected, lysed, and

rifampicin concentrations determined using an appropriate quantitative methodology such as high-performance liquid chromatography (Chuan et al., 2012). Pharmacological efficacy of rifampicin-containing NPs can be assessed by histopathological examination of the lungs and microbiological determination of viable bacteria (Suarez et al., 2001).

In an expansion of the current research, it is also important to explore future opportunities of this nanotechnology-based SMART drug delivery system for hydrophilic anti-TB drugs, including, but not limited to, INH and streptomycin.

8. References

Abulateefeh, Samer R., Sebastian G. Spain, Jonathan W. Aylott, Weng C. Chan, Martin C. Garnett, and Cameron Alexander. 2011. "Thermoresponsive Polymer Colloids for Drug Delivery and Cancer Therapy." *Macromolecular Bioscience* 11 (12): 1722-1734.

Allam, Ayat A., Md Ehsan Sadat, Sarah J. Potter, David B. Mast, Dina F. Mohamed, Fawzia S. Habib, and Giovanni M. Pauletti. 2013. "Stability and Magnetically Induced Heating Behavior of Lipid-Coated Fe₃O₄ Nanoparticles." *Nanoscale Research Letters* 8 (1): 1-7.

Anisimova, YV, SI Gelperina, CA Peloquin, and LB Heifets. 2000. "Nanoparticles as Antituberculosis Drugs Carriers: Effect on Activity against Mycobacterium Tuberculosis in Human Monocyte-Derived Macrophages." *Journal of Nanoparticle Research* 2 (2): 165-171.

Baciewicz, A. M. and T. H. Self. 1984. "Rifampin Drug Interactions." *Archives of Internal Medicine* 144 (8): 1667-1671.

Baker, Richard William. 1987. *Controlled Release of Biologically Active Agents*. John Wiley & Sons. 1-18. Elsevier, 2012

Bennet, Devasier and Sanghyo Kim. 2014. "Polymer Nanoparticles for Smart Drug Delivery."

Bermudez, L. E. and J. Goodman. 1996. "Mycobacterium Tuberculosis Invades and Replicates within Type II Alveolar Cells." *Infection and Immunity* 64 (4): 1400-1406.

Bharathi, M., SCM Prasad, RL Eswari, S. Wajim Raja, RT Allena, S. Brito Raj, and K. Bhaskar Reddy. 2012. "Preparation and in Vitro & in Vivo Characterization of Valsartan Loaded Eudragit Nanoparticles." *Der Pharmacia Sinica* 3 (5): 516-525.

Billmeyer Jr, Fred W. "Textbook of Polymer Science, 1984." *New York*. 151-153. A Wiley-Interscience Publication

Brennan, Patrick J. 2003. "Structure, Function, and Biogenesis of the Cell Wall of Mycobacterium Tuberculosis." *Tuberculosis* 83 (1): 91-97.

Bryk, R., C. D. Lima, H. Erdjument-Bromage, P. Tempst, and C. Nathan. 2002. "Metabolic Enzymes of Mycobacteria Linked to Antioxidant Defense by a Thioredoxin-Like Protein." *Science (New York, N.Y.)* 295 (5557): 1073-1077.

Bullo Saifullah, Mohd Zobir B Hussein and Al Ali, Samer Hasan Hussein. 2012. "Controlled-Release Approaches towards the Chemotherapy of Tuberculosis." *International Journal of Nanomedicine* 7: 5451.

Butor, C., G. Griffiths, N. N. Aronson Jr, and A. Varki. 1995. "Co-Localization of Hydrolytic Enzymes with Widely Disparate pH Optima: Implications for the Regulation of Lysosomal pH." *Journal of Cell Science* 108 (Pt 6) (Pt 6): 2213-2219.

Castañeda-Hernández, Diana M. and Alfonso J. Rodriguez-Morales. 2013. "Epidemiological Burden of Tuberculosis in Developing Countries." "Current Topics in Public Health", edited by Alfonso J. Rodriguez-Morales, Published: May 15, 2013.

Chuan, Junlan, Yanzhen Li, Likai Yang, Xun Sun, Qiang Zhang, Tao Gong, and Zhirong Zhang. 2013. "Enhanced Rifampicin Delivery to Alveolar Macrophages by Solid Lipid Nanoparticles." *Journal of Nanoparticle Research* 15 (5): 1-9.

Chung, Chiu-Yen, Jen-Tsung Yang, and Yung-Chih Kuo. 2013. "Polybutylcyanoacrylate Nanoparticles for Delivering Hormone Response Element-Conjugated Neurotrophin-3 to the Brain of Intracerebral Hemorrhagic Rats." *Biomaterials* 34 (37): 9717-9727.

Ddbst. 2015. The Dortmund Data Bank
ddbonline.ddbst.com/AntoineCalculation/AntoineCalculationCGI.exe?component=Acetone
accessed 7/19/2015

De Duve, C. and J. Berthet. 1953. "Reproducibility of Differential Centrifugation Experiments in Tissue Fractionation."

De Duve, Christian, Thierry De Barse, Brian Poole, and Paul Tulkens. 1974. "Lysosomotropic Agents." *Biochemical Pharmacology* 23 (18): 2495-2531.

De La Rica, Roberto, Daniel Aili, and Molly M. Stevens. 2012. "Enzyme-Responsive Nanoparticles for Drug Release and Diagnostics." *Advanced Drug Delivery Reviews* 64 (11): 967-978.

DesJardin, L. E., T. M. Kaufman, B. Potts, B. Kutzbach, H. Yi, and L. S. Schlesinger. 2002. "Mycobacterium Tuberculosis-Infected Human Macrophages Exhibit Enhanced Cellular Adhesion with Increased Expression of LFA-1 and ICAM-1 and Reduced Expression and/or Function of Complement Receptors, FcγRII and the Mannose Receptor." *Microbiology (Reading, England)* 148 (Pt 10): 3161-3171.

Devarajan, Padma V. and Ganeshchandra S. Sonavane. 2007. "Preparation and in vitro/in Vivo Evaluation of Gliclazide Loaded Eudragit Nanoparticles as a Sustained Release Carriers." *Drug Development and Industrial Pharmacy* 33 (2): 101-111.

Doherty, Gary J. and Harvey T. McMahon. 2009. "Mechanisms of Endocytosis." *Annual Review of Biochemistry* 78: 857-902.

Du Toit, Lisa Claire, Viness Pillay, and Michael Paul Danckwerts. 2006. "Tuberculosis Chemotherapy: Current Drug Delivery Approaches." *Respir Res* 7 (1): 118.

Eidi, Housam, Olivier Joubert, Christophe Némos, Stéphanie Grandemange, Baharia Mograbi, Bernard Foliguet, Juliana Tournebize, Philippe Maincent, Alain Le Faou, and Imad Aboukhamis. 2012. "Drug Delivery by Polymeric Nanoparticles Induces Autophagy in Macrophages." *International Journal of Pharmaceutics* 422 (1): 495-503.

Fawaz, F., F. Bonini, J. Maugein, and AM Lagueny. 1998. "Ciprofloxacin-Loaded Polyisobutylcyanoacrylate Nanoparticles: Pharmacokinetics and in Vitro Antimicrobial Activity." *International Journal of Pharmaceutics* 168 (2): 255-259.

Fenton, Matthew J., Lee W. Riley, and Larry S. Schlesinger. 2005. "Receptor-Mediated Recognition of Mycobacterium Tuberculosis by Host Cells." *Tuberculosis and the Tubercle Bacillus* / Chapter 25. Editors: Stewart T. Cole, Kathleen Davis Eisenach, David N. McMurray, William R. Jacobs, Jr.

Ferrari, Giorgio, Hanno Langen, Makoto Naito, and Jean Pieters. 1999. "A Coat Protein on Phagosomes Involved in the Intracellular Survival of Mycobacteria." *Cell* 97 (4): 435-447.

Foss, Aaron C., Takahiro Goto, Mariko Morishita, and Nicholas A. Peppas. 2004. "Development of Acrylic-Based Copolymers for Oral Insulin Delivery." *European Journal of Pharmaceutics and Biopharmaceutics* 57 (2): 163-169.

Geisow, M. J., P. D'Arcy Hart, and M. R. Young. 1981. "Temporal Changes of Lysosome and Phagosome pH during Phagolysosome Formation in Macrophages: Studies by Fluorescence Spectroscopy." *The Journal of Cell Biology* 89 (3): 645-652.

Gelperina, Svetlana, Kevin Kisich, Michael D. Iseman, and Leonid Heifets. 2005. "The Potential Advantages of Nanoparticle Drug Delivery Systems in Chemotherapy of Tuberculosis." *American Journal of Respiratory and Critical Care Medicine* 172 (12): 1487-1490.

Gupta, Antima, Akshay Kaul, Anthony G. Tsolaki, Uday Kishore, and Sanjib Bhakta. 2012. "Mycobacterium Tuberculosis: Immune Evasion, Latency and Reactivation." *Immunobiology* 217 (3): 363-374.

Hackam, David J., Ori D. Rotstein, Wei-Jian Zhang, Nicolas Demaurex, Michael Woodside, Olivia Tsai, and Sergio Grinstein. 1997. "Regulation of Phagosomal Acidification Differential Targeting of Na⁺/H Exchangers, Na⁺/K⁺-ATPases, and Vacuolar-Type H⁺-ATPases." *Journal of Biological Chemistry* 272 (47): 29810-29820.

- Hanafi, Aimi, Nadine Nograles, Syahril Abdullah, Mariana Nor Shamsudin, and Rozita Rosli. 2013. "Cellulose Acetate Phthalate Microencapsulation and Delivery of Plasmid DNA to the Intestines." *Journal of Pharmaceutical Sciences* 102 (2): 617-626.
- Hixson, AW and JH Crowell. 1931. "Dependence of Reaction Velocity upon Surface and Agitation." *Industrial & Engineering Chemistry* 23 (10): 1160-1168.
- Holdiness, Mack R. 1984. "Clinical Pharmacokinetics of the Antituberculosis Drugs." *Clinical Pharmacokinetics* 9 (6): 511-544.
- Huang, Yi-Shin, Heng-Der Chern, Wei-Juin Su, Jaw-Ching Wu, Shinn-Liang Lai, Shi-Yi Yang, Full-Young Chang, and Shou-Dong Lee. 2002. "Polymorphism of the N-Acetyltransferase 2 Gene as a Susceptibility Risk Factor for Antituberculosis drug-induced Hepatitis." *Hepatology* 35 (4): 883-889.
- Huang, Yi-You and Ching-Hua Wang. 2006. "Pulmonary Delivery of Insulin by Liposomal Carriers." *Journal of Controlled Release* 113 (1): 9-14.
- Ivanov, Andrei I. 2008. "Pharmacological Inhibition of Endocytic Pathways: Is it Specific enough to be Useful?" In *Exocytosis and Endocytosis*, 15-33: Springer.
- Kang, P. B., A. K. Azad, J. B. Torrelles, T. M. Kaufman, A. Beharka, E. Tibesar, L. E. DesJardin, and L. S. Schlesinger. 2005. "The Human Macrophage Mannose Receptor Directs Mycobacterium Tuberculosis Lipoarabinomannan-Mediated Phagosome Biogenesis." *The Journal of Experimental Medicine* 202 (7): 987-999.
- Karve, S., M. E. Werner, N. D. Cummings, R. Sukumar, E. C. Wang, Y. A. Zhang, and A. Z. Wang. 2011. "Formulation of Diblock Polymeric Nanoparticles through Nanoprecipitation Technique." *Journal of Visualized Experiments : JoVE* (55). pii: 3398. doi (55): 10.3791/3398.
- Kaufmann, Stefan HE. 2001. "How can Immunology Contribute to the Control of Tuberculosis?" *Nature Reviews Immunology* 1 (1): 20-30.
- Khan, M. Zahirul I., Helena P. Štedul, and Nevenka Kurjaković. 2000. "A pH-Dependent Colon-Targeted Oral Drug Delivery System using Methacrylic Acid Copolymers. II. Manipulation of Drug Release using Eudragit® L100 and Eudragit S100 Combinations." *Drug Development and Industrial Pharmacy* 26 (5): 549-554.
- Klaikherd, Akamol, Chikkannagari Nagamani, and Sankaran Thayumanavan. 2009. "Multi-Stimuli Sensitive Amphiphilic Block Copolymer Assemblies." *Journal of the American Chemical Society* 131 (13): 4830-4838.
- Korsmeyer, Richard W., Robert Gurny, Eric Doelker, Pierre Buri, and Nikolaos A. Peppas. 1983. "Mechanisms of Solute Release from Porous Hydrophilic Polymers." *International Journal of Pharmaceutics* 15 (1): 25-35.

Kreuter J. Nanoparticles as drug delivery system. In: Nalwa HS, editor. Encyclopedia of nanoscience and nanotechnology. Vol. 7. New York: American Scientific Publishers; 2004. pp. 161–180.

Kuhn, Dagmar A., Dimitri Vanhecke, Benjamin Michen, Fabian Blank, Peter Gehr, Alke Petri-Fink, and Barbara Rothen-Rutishauser. 2014. "Different Endocytotic Uptake Mechanisms for Nanoparticles in Epithelial Cells and Macrophages." *Beilstein Journal of Nanotechnology* 5 (1): 1625-1636.

Kwon, Ick Chan, You Han Bae, and Sung Wan Kim. 1991. "Electrically Credible Polymer Gel for Controlled Release of Drugs."

Labiris, NR and MB Dolovich. 2003. "Pulmonary Drug Delivery. Part I: Physiological Factors Affecting Therapeutic Effectiveness of Aerosolized Medications." *British Journal of Clinical Pharmacology* 56 (6): 588-599.

Lee, Sang-Min and SonBinh T. Nguyen. 2013. "Smart Nanoscale Drug Delivery Platforms from Stimuli-Responsive Polymers and Liposomes." *Macromolecules* 46 (23): 9169-9180.

Lodish, Harvey, Arnold Berk, S. Lawrence Zipursky, Paul Matsudaira, David Baltimore, and James Darnell. 2000. "Purifying, Detecting, and Characterizing Proteins." *Molecular Cell Biology*. 4th edition. New York: W. H. Freeman; 2000.

Meng, Fenghua, Wim E. Hennink, and Zhiyuan Zhong. 2009. "Reduction-Sensitive Polymers and Bioconjugates for Biomedical Applications." *Biomaterials* 30 (12): 2180-2198.

Mikusova, K., R. A. Slayden, G. S. Besra, and P. J. Brennan. 1995. "Biogenesis of the Mycobacterial Cell Wall and the Site of Action of Ethambutol." *Antimicrobial Agents and Chemotherapy* 39 (11): 2484-2489.

Moulder, J. W. 1985. "Comparative Biology of Intracellular Parasitism." *Microbiological Reviews* 49 (3): 298-337.

NIH. 2012. Accessed 7/19/2015

<http://www.nih.gov/researchmatters/january2011/01242011nanoparticles.htm>.

NIH. 2015. "New Tuberculosis (TB) Drugs in Development, Drug-Resistant TB—A Visual Tour, NIAID, NIH ", accessed 7/11/2015,

<http://www.niaid.nih.gov/topics/tuberculosis/Understanding/WhatIsTB/VisualTour/pages/newdrugs.aspx>

Nuutila, Jari and Esa-Matti Lilius. 2005. "Flow Cytometric Quantitative Determination of Ingestion by Phagocytes Needs the Distinguishing of Overlapping Populations of Binding and Ingesting Cells." *Cytometry Part A* 65 (2): 93-102.

- Ohkuma, S. and B. Poole. 1978. "Fluorescence Probe Measurement of the Intralysosomal pH in Living Cells and the Perturbation of pH by various Agents." *Proceedings of the National Academy of Sciences of the United States of America* 75 (7): 3327-3331.
- Pandey, Rajesh and GK Khuller. 2005. "Solid Lipid Particle-Based Inhalable Sustained Drug Delivery System Against Experimental Tuberculosis." *Tuberculosis* 85 (4): 227-234.
- Pandey, R., A. Sharma, A. Zahoor, S. Sharma, G. K. Khuller, and B. Prasad. 2003. "Poly (DL-Lactide-Co-Glycolide) Nanoparticle-Based Inhalable Sustained Drug Delivery System for Experimental Tuberculosis." *The Journal of Antimicrobial Chemotherapy* 52 (6): 981-986.
- Poole, B. and S. Ohkuma. 1981. "Effect of Weak Bases on the Intralysosomal pH in Mouse Peritoneal Macrophages." *The Journal of Cell Biology* 90 (3): 665-669.
- Rejinold, N. Sanoj, M. Muthunayanan, VV Divyarani, PR Sreerexha, KP Chennazhi, SV Nair, H. Tamura, and R. Jayakumar. 2011. "Curcumin-Loaded Biocompatible Thermoresponsive Polymeric Nanoparticles for Cancer Drug Delivery." *Journal of Colloid and Interface Science* 360 (1): 39-51.
- Russell, DAVID G. 2005. "Mycobacterium Tuberculosis: The Indigestible Microbe." *Tuberculosis and the Tubercle Bacillus*: 427-435.
- Sahay, Gaurav, Daria Y. Alakhova, and Alexander V. Kabanov. 2010. "Endocytosis of Nanomedicines." *Journal of Controlled Release* 145 (3): 182-195.
- Santa Cruz Biotechnology (2015). Accessed 7/19/2015
<http://www.scbt.com/datasheet-200910-rifampicin.html>
<http://www.scbt.com/datasheet-208306-rhodamine-123.html>
- Schlesinger, L. S. 1993. "Macrophage Phagocytosis of Virulent but Not Attenuated Strains of Mycobacterium Tuberculosis is Mediated by Mannose Receptors in Addition to Complement Receptors." *Journal of Immunology (Baltimore, Md.: 1950)* 150 (7): 2920-2930.
- Shoeb, H. A., B. U. Bowman Jr, A. C. Ottolenghi, and A. J. Merola. 1985. "Peroxidase-Mediated Oxidation of Isoniazid." *Antimicrobial Agents and Chemotherapy* 27 (3): 399-403.
- Smith, J. P. 2011. "Nanoparticle Delivery of Anti-Tuberculosis Chemotherapy as a Potential Mediator Against Drug-Resistant Tuberculosis." *The Yale Journal of Biology and Medicine* 84 (4): 361-369.
- St John, G., N. Brot, J. Ruan, H. Erdjument-Bromage, P. Tempst, H. Weissbach, and C. Nathan. 2001. "Peptide Methionine Sulfoxide Reductase from Escherichia Coli and Mycobacterium Tuberculosis Protects Bacteria Against Oxidative Damage from Reactive Nitrogen Intermediates." *Proceedings of the National Academy of Sciences of the United States of America* 98 (17): 9901-9906.

- Sturgill-Koszycki, S., P. H. Schlesinger, P. Chakraborty, P. L. Haddix, H. L. Collins, A. K. Fok, R. D. Allen, S. L. Gluck, J. Heuser, and D. G. Russell. 1994. "Lack of Acidification in Mycobacterium Phagosomes Produced by Exclusion of the Vesicular Proton-ATPase." *Science (New York, N.Y.)* 263 (5147): 678-681.
- Suarez, S., P. O'Hara, M. Kazantseva, C. E. Newcomer, R. Hopfer, D. N. McMurray, and A. J. Hickey. 2001. "Airways Delivery of Rifampicin Microparticles for the Treatment of Tuberculosis." *The Journal of Antimicrobial Chemotherapy* 48 (3): 431-434.
- Taghizadeh, Bitra, Shahrouz Taranejoo, Seyed Ali Monemian, Zoha Salehi Moghaddam, Karim Daliri, Hossein Derakhshankhah, and Zaynab Derakhshani. 2015. "Classification of Stimuli-Responsive Polymers as Anticancer Drug Delivery Systems." *Drug Delivery* 22 (2): 145-155.
- Talelli, Marina, Maryam Iman, Amir K. Varkouhi, Cristianne JF Rijcken, Raymond M. Schiffelers, Tomas Etrych, Karel Ulbrich, Cornelus F. van Nostrum, Twan Lammers, and Gert Storm. 2010. "Core-Crosslinked Polymeric Micelles with Controlled Release of Covalently Entrapped Doxorubicin." *Biomaterials* 31 (30): 7797-7804.
- Tang, J., N. Xu, H. Ji, H. Liu, Z. Wang, and L. Wu. 2011. "Eudragit Nanoparticles Containing Genistein: Formulation, Development, and Bioavailability Assessment." *International Journal of Nanomedicine* 6: 2429-2435.
- Thambi, Thavasyappan, VG Deepagan, Hong Yeol Yoon, Hwa Seung Han, Seol-Hee Kim, Soyong Son, Dong-Gyu Jo, Cheol-Hee Ahn, Yung Doug Suh, and Kwangmeyung Kim. 2014. "Hypoxia-Responsive Polymeric Nanoparticles for Tumor-Targeted Drug Delivery." *Biomaterials* 35 (5): 1735-1743.
- Torrelles, Jordi B. and Larry S. Schlesinger. 2010. "Diversity in Mycobacterium Tuberculosis Mannosylated Cell Wall Determinants Impacts Adaptation to the Host." *Tuberculosis* 90 (2): 84-93.
- van Crevel, R., T. H. Ottenhoff, and J. W. van der Meer. 2002. "Innate Immunity to Mycobacterium Tuberculosis." *Clinical Microbiology Reviews* 15 (2): 294-309.
- Vaupel, P., F. Kallinowski, and P. Okunieff. 1989. "Blood Flow, Oxygen and Nutrient Supply, and Metabolic Microenvironment of Human Tumors: A Review." *Cancer Research* 49 (23): 6449-6465.
- Veksler, BA, A. Lemelle, IS Kozhevnikov, GG Akchurin, and IV Meglinski. 2011. "Improving Image Quality in Reflection Confocal Microscopy Involving Gold Nanoparticles and Osmotically Active Immersion Liquids." *Optics and Spectroscopy* 110 (3): 483-488.
- Walker, Roger and Cate Whittlesea. 2011. *Clinical Pharmacy and Therapeutics* Elsevier Health Sciences.

Wang, Yan, Bing Gu, and Diane J. Burgess. 2014. "Microspheres Prepared with PLGA Blends for Delivery of Dexamethasone for Implantable Medical Devices." *Pharmaceutical Research* 31 (2): 373-381.

Wong, D., H. Bach, J. Sun, Z. Hmama, and Y. Av-Gay. 2011. "Mycobacterium Tuberculosis Protein Tyrosine Phosphatase (PtpA) Excludes Host Vacuolar-H⁺-ATPase to Inhibit Phagosome Acidification." *Proceedings of the National Academy of Sciences of the United States of America* 108 (48): 19371-19376.

World Health Organization (2015). <http://www.who.int/features/qa/79/en/>. Accessed 7/20/2015

World Health Organization. 2010. "Multidrug and Extensively Drug-Resistant TB." .

Xiong, Ranhua, Stefaan J. Soenen, Kevin Braeckmans, and Andre G. Skirtach. 2013. "Towards Theranostic Multicompartment Microcapsules: In-Situ Diagnostics and Laser-Induced Treatment." *Theranostics* 3 (3): 141.

Yang, Chul-Su, Jae-Min Yuk, and Eun-Kyeong Jo. 2009. "The Role of Nitric Oxide in Mycobacterial Infections." *Immune Network* 9 (2): 46-52.

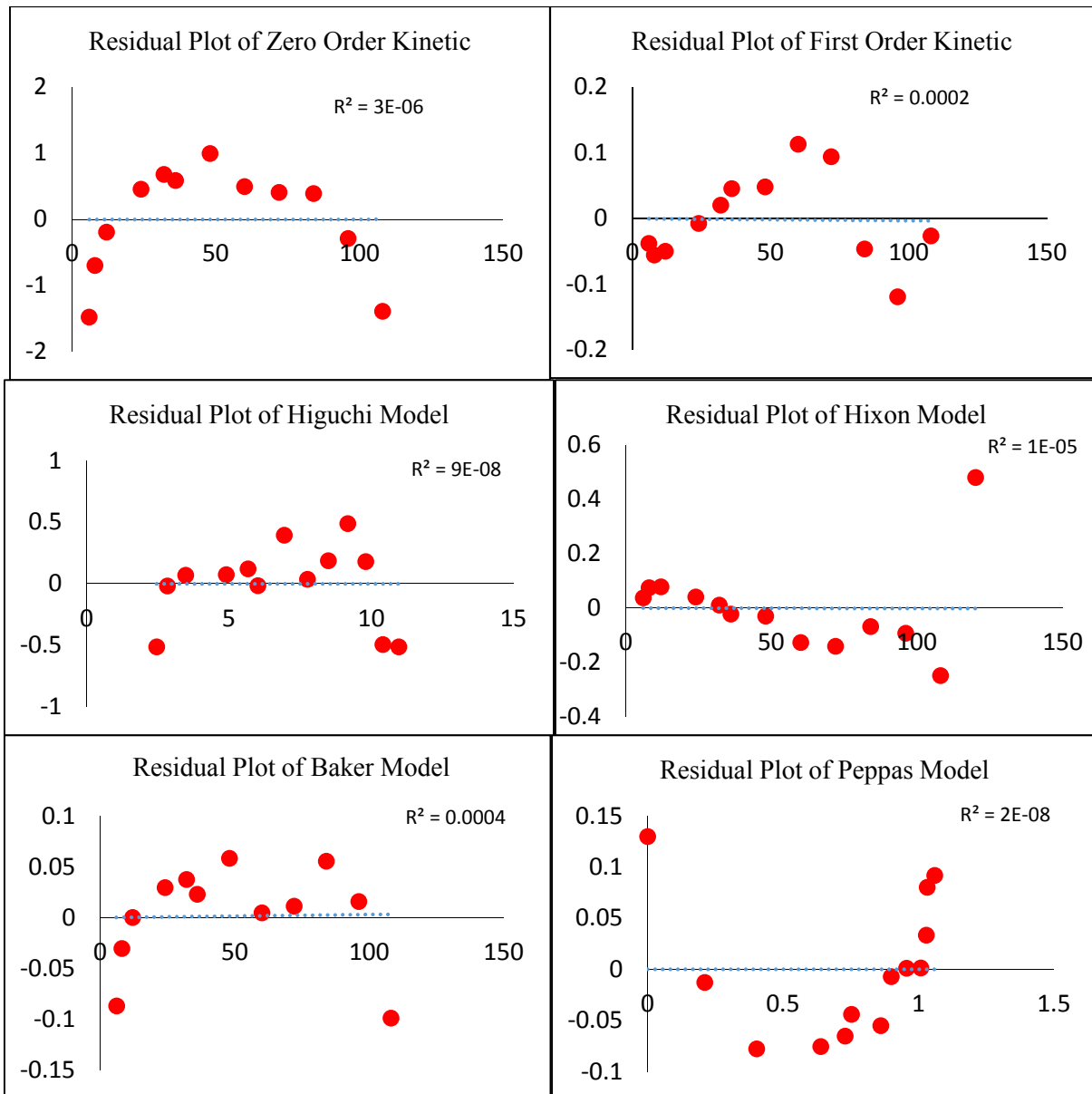
Yuan, Y., R. E. Lee, G. S. Besra, J. T. Belisle, and C. E. Barry 3rd. 1995. "Identification of a Gene Involved in the Biosynthesis of Cyclopropanated Mycolic Acids in Mycobacterium Tuberculosis." *Proceedings of the National Academy of Sciences of the United States of America* 92 (14): 6630-6634.

Zhang, Y., M. M. Wade, A. Scorpio, H. Zhang, and Z. Sun. 2003. "Mode of Action of Pyrazinamide: Disruption of Mycobacterium Tuberculosis Membrane Transport and Energetics by Pyrazinoic Acid." *The Journal of Antimicrobial Chemotherapy* 52 (5): 790-795.

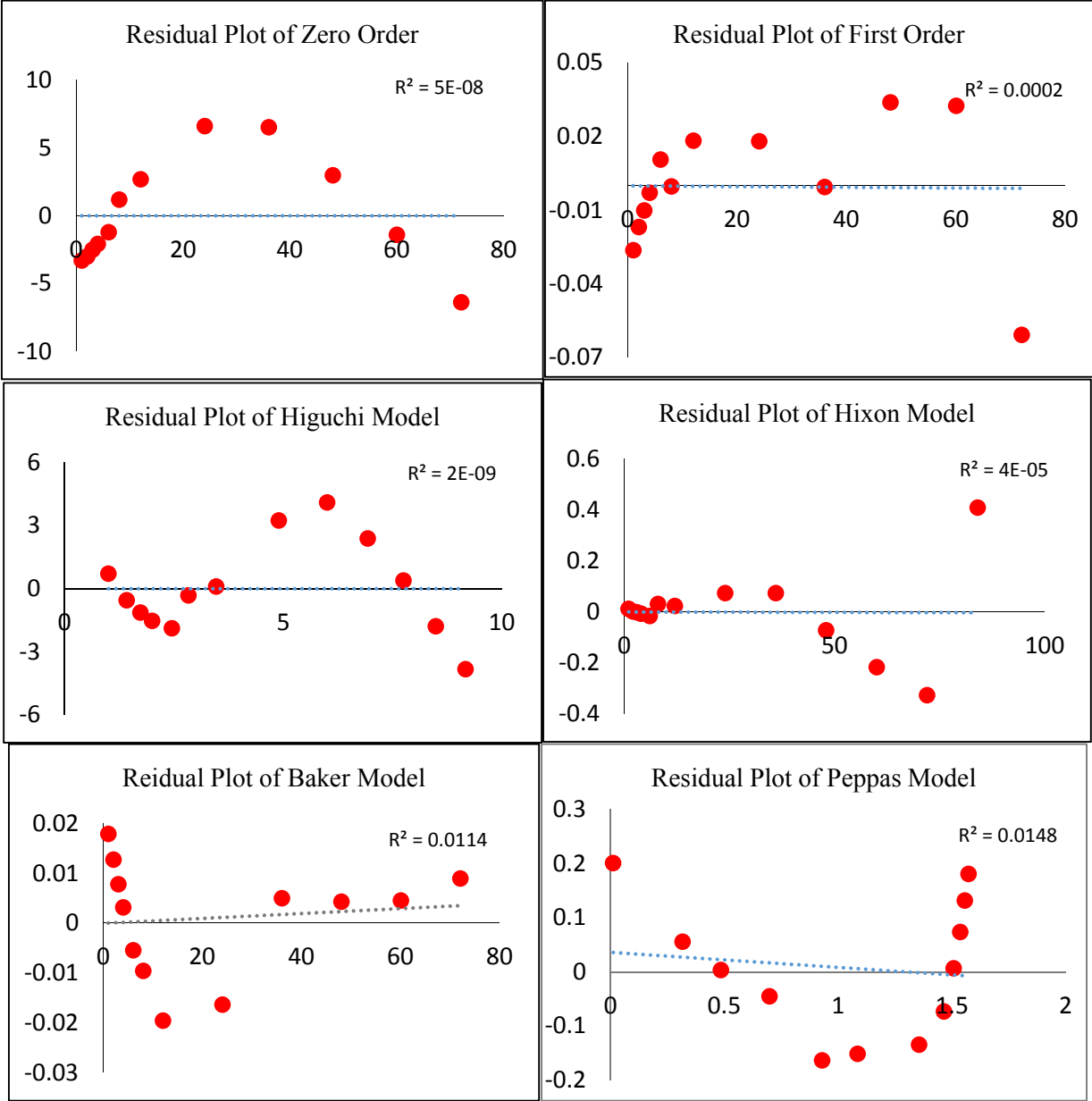
APPENDIX

Residuals Plots generated from regression analyses performed with different mathematical models using pH-dependent Rh123 release data.

a) pH 5.5



b) pH 6.2



c) pH 7.4

